

EXCIMER-LASER CRYSTALLIZATION OF
AMORPHOUS SILICON THIN FILMS

By

JOHN VIATELLA

A DISSERTATION PRESENTED TO THE GRADUATE SCHOOL
OF THE UNIVERSITY OF FLORIDA IN PARTIAL FULFILLMENT
OF THE REQUIREMENTS FOR THE DEGREE OF
DOCTOR OF PHILOSOPHY

UNIVERSITY OF FLORIDA

1997

To my mother, for her love and support.

ACKNOWLEDGMENTS

I would like to acknowledge the many individuals that have made this work possible. First, I would like to thank my advisor, Dr. Rajiv K. Singh, for his guidance, support and encouragement. The open environment that he has provided over the years that I have worked with him has made for a very dynamic and rewarding graduate school experience. I would also like to thank Dr. Paul Holloway, Dr. Robert Park, Dr. Steve Pearton, and Dr. Mark Law for kindly participating on my dissertation committee.

Several people played an important role in assisting me with my research. Thanks especially go to Don Gilbert for providing many hours of discussion, both technical and philosophical, without which the graduate school experience would have been greatly lessened. Thanks are also due to Brent Gila for friendship and extensive technical assistance with TEM sample preparation.

I would like to also acknowledge all the friends and coworkers who made graduate school such a memorable time. Brock, Sam, Bark, Rich, Fan, Rajan, Jeff T., Troy, Jeff D., Karen, Chummy, Dong Gu, Chris, Mike, and others provided the

social perspective that is always necessary in life. Special thanks go to Kathy Cochran for her support and encouragement during the preparation of this dissertation.

Thanks are due to the National Science Foundation's MEDI Fellowship which has provided the resources to make the work possible. Dr. Warren Viessman's support and encouragement in organizing the fellowship is especially appreciated.

I would also like to thank the administrative and support staff of the Department of Materials Science and Engineering for their efforts in making success possible.

Finally, I would like to thank my mother, my brother and the rest of my family for the love and support they have provided over the many years of my extended education.

TABLE OF CONTENTS

ACKNOWLEDGMENTS	iii
ABSTRACT	vii
CHAPTER 1 INTRODUCTION	1
Background and Motivation	1
Dissertation Outline	3
CHAPTER 2 LITERATURE REVIEW	5
Introduction	5
Excimer Lasers	5
Discharge Physics..	8
Beam Profile	9
Laser-Solid Interactions	10
Silicon Thin Film Technology	16
Applications	17
Thin Film Transistor (TFT) Structure	20
Effects of Microstructure on TFTs	20
TFT Processing Techniques	25
Laser Crystallization of Silicon Thin Films	28
Optical and Thermophysical Properties of Si	28
Mechanisms in Pulsed Laser Crystallization	31
Previous Work	37
CHAPTER 3 EXPERIMENTAL APPROACH	67
Introduction	67
Samples	68
Laser Setup	69
Seeded Nucleation Experiments	70
Seed Wafers	70
Native Oxide Removal	72
Laser Processing	74
Selective Crystallized Area Experiments	75
Mask Configurations and Laser Parameters	76
Transmission Electron Microscopy (TEM)	77
Scanning Electron Microscopy (SEM)	79
CHAPTER 4 RESULTS	88
Seeded Nucleation Experiments	88
Seed Wafers	88
Crystallized Samples.	88
Selective Crystallized Area Experiments	90
Contact Samples	91

Non-Contact Samples	94
Variable Apperture Area Samples	97
CHAPTER 5 DISCUSSION	129
Solidification of Laser-Melted Silicon Films	129
Thermodynamics	129
Kinetics	132
Interface Response Function	133
Seeded Nucleation Experiments	136
Selective Crystallized Area Experiments	139
Evolution of Microstructure	140
Anomalous Microstructures	149
Non-contact Samples	150
CHAPTER 6 CONCLUSIONS	160
APPENDIX SIMULATION OF LASER INTERACTIONS WITH MATERIALS	162
LIST OF REFERENCES	165
BIOGRAPHICAL SKETCH	173

Abstract of Dissertation Presented to the Graduate School
of the University of Florida in Partial Fulfillment of the
Requirements for the Degree of Doctor of Philosophy

EXCIMER-LASER CRYSTALLIZATION OF
AMORPHOUS SILICON THIN FILMS

By

John Viatella

May, 1997

Chairperson: Rajiv K. Singh

Major Department: Materials Science and Engineering

Amorphous silicon films deposited on high-quality fused-silica wafers were crystallized using an excimer laser. Two unique configurations were used for the crystallization process. They were (i) through-the substrate irradiation using special seed wafers in contact with the film surface and (ii) selective-area crystallization using surface masking of the film during standard laser irradiation. The resultant microstructure of the films was then characterized by transmission electron microscopy (TEM) and scanning electron microscopy (SEM).

Samples processed using the seed method resulted in structures in which the film in contact with the seed delaminated, leaving behind a unique microstructure. Four distinct regions were observed, as a function of lateral

distance from the contact area. Regions at least several microns away from the seed did not demonstrate any effect (grain size ~ 200 nm, no aspect ratio), but regions closer demonstrated enlarged growth (~ 1 μm , aspect ratio 2:1) due to the nucleation effect caused by the seed.

Samples processed using selective-area crystallization of the film resulted in one of three microstructures. Samples processed with the lower laser energy densities (200-300 mJ/cm^2) demonstrated a microstructure consistent with regular laser annealing (grain size ~ 200 nm, no aspect ratio). Samples processed with higher energy densities (300-470 mJ/cm^2) demonstrated either enlarged grain growth (factor of 3 greater than standard annealing), or anomalous grain growth (unusual aspect ratio or geometry).

CHAPTER 1 INTRODUCTION

Background and Motivation

Lasers are a unique and useful tool for processing metals, semiconductors, and ceramics [Sin92]. Laser processing of materials emerged as a viable technique primarily during the 1970s [Aus78, Liu79, Sir79, Tsu79], though there was work done in the study of laser interactions with solids in the 1960s [Rea63].

One area that has generated much interest involves annealing of deposited amorphous silicon (a-Si) films for semiconductor technology [Bro93, Bac90, Bou92, Cho94a, Fog93]. Laser annealing has been investigated because the fast heating and cooling rates minimize dopant redistribution and limit the high temperatures to surface layers [Liu79], preventing damage to underlying structures. Nd:YAG [Sir79] and ruby lasers [Cul82] operating in nanosecond-regime pulse lengths have been used in this type of processing. During the 1980s, however, technical improvements of excimer lasers allowed them to become popular for materials processing [Sam86, Sam87]. The

intense output and high frequency that the excimers are capable of makes them particularly appealing in the area of semiconductor technology. Use of excimer lasers in silicon annealing has therefore been actively investigated [Bac90, Bro93, Cho94, Dye93, Hol92, Im93, Kur93, Lar88, Sam91].

One area where laser annealing is particularly well suited is in large-area electronics-on-glass applications [Bac90]. Typically, a silicon film is deposited on the transparent substrates at temperatures less than 600°C, due to the temperature-processing limit of the glass, resulting in an amorphous film. After an anneal step, thin-film transistors (TFTs) are fabricated on the film. The fabrication of these TFTs on a transparent substrate lies at the heart of active-matrix liquid-crystal-display (AMLCD) technology [Oma93]. Applications for this technology include direct-view displays for laptop computers [Haj94], light-shutter based projection displays, and small displays such as video camera viewfinders [Yam94].

Currently, the technology that is most advanced takes advantage of TFTs fabricated on the as-deposited amorphous film because lower processing temperatures are used compared to polycrystalline films [Bro93]. However, channel mobilities of TFT's on amorphous silicon are quite low [Ive87], less than $1 \text{ cm}^2/\text{V}\cdot\text{s}$. Channel mobility on polycrystalline silicon is higher than that for amorphous silicon, but lower than single

crystal because of grain boundary effects. One method of reducing the grain boundary effects is by increasing grain size through an annealing step. Many techniques have therefore been investigated, including furnace annealing [Bon91], rapid thermal processing [Haj94], and laser annealing [Bro93].

Laser annealing of amorphous silicon thin films has been actively investigated [Ser89] because the process results in the highest carrier-mobility values observed, when compared to furnace annealing [Sag89] and rapid thermal processing [Kak89]. However, much work remains in understanding the transformation mechanisms [Im93]. Also, there is a desire to control the number of grain boundaries, specifically in the active channel region of devices. Hence, though laser annealing presents itself as a lucrative technique due to the resultant electrical properties, there is much work to be done in understanding the microstructural evolution of the crystallized films.

Dissertation Outline

The objective of this study was to investigate the evolution of microstructure of laser-annealed amorphous silicon thin films in two unique configurations. The conditions during the crystallization were (i) through-the-

substrate irradiation using special silicon seed wafers in contact with the film surface, and (ii) selective-area crystallization using surface-masking of the film during standard laser irradiation. The resultant microstructure of the films was then characterized by transmission electron microscopy (TEM) and scanning electron microscopy (SEM).

Chapter 2 first gives a general review on the subject of laser annealing of silicon thin films. This includes the physics of excimer lasers and laser-solid interactions. Mechanisms in laser crystallization of amorphous films are also discussed, including relevant aspects of the optical and thermophysical properties of silicon.

Chapter 3 accounts the experimental procedure used in this study. Chapter 4 presents the results of the experiments, followed by a discussion of those results in Chapter 5. The conclusions of the study are given in Chapter 6.

CHAPTER 2 LITERATURE REVIEW

Introduction

As mentioned in Chapter 1, laser annealing of amorphous silicon thin films has been actively investigated due to the excellent electrical properties of the crystallized films.

In this chapter, literature pertaining to excimer laser crystallization of silicon thin films is reviewed. The chapter begins with a discussion of excimer lasers and laser-solid interactions. This is followed by a discussion of silicon thin film technology including applications, thin film transistor structure and processing techniques. The rest of the chapter is devoted to mechanisms of laser crystallization of thin films, including a discussion of the optical and thermophysical properties of silicon.

Excimer Lasers

The concept of bound-free excimer system as a laser medium was initially brought forth in 1960, though the first

successful laboratory demonstrations were not accomplished until 1972 [Hof79]. Excimer lasers are defined as gas lasers that derive their output from a molecular gain medium in which the photon emission occurs during the transition from a bound upper electronic state to a repulsive and weakly bound ground electronic state [Chr94]. Use of different gases results in different output frequency, with output typically in the ultra-violet (UV) regime (198-308 nm).

Ten rare gas monohalide species have been observed, of which six have exhibited stimulated emission [Bra79]. Four of these have been observed to oscillate rather efficiently, namely ArF, KrF, XeCl and XeF. The krypton-fluoride (KrF) mixture is commonly used, including this work, because it represents the highest gain system for electrically-discharged pumped, rare gas halogen excimer lasers [Chr94]. The reaction kinetics for the rare gas halide lasers are complex, involving several ground state atomic and molecular species, several ionic species, and a large number of excited atomic and molecular species, but enough has been learned to describe the most important aspects of performance. First, a discussion of the rare-gas halide reactions is provided, followed by a discussion of discharge physics, concluding with current laser configurations and beam profiles.

Though details of the complete process of photon generation in excimer lasers are complex and consist of many

steps, a general description can be given. The excimer molecules are formed in a gas mixture of the components as well as buffer gases. For example, a KrF system typically will consist of ~ 4% Kr, ~ 0.4% F, and the remainder neon as a buffer gas. The species exist atomically or diatomically and remain in a repulsive ground state until excited electronically through avalanche electric-discharge excitation. The ionic and excited species then react chemically and produce the excimer molecules. Once formed, the molecules will decay via spontaneous emission and collisional deactivation, giving the molecule a lifetime of ~ 2.5 ns.

Electrical excitation of predominantly rare gas mixtures results in production of both excited rare gas atoms and rare gas ions [Bra79],



and



Both of these products lead very rapidly to excited rare gas halides by direct reaction,



where Kr is krypton, F is fluorine, X denotes a third body (helium, neon) and the asterisk indicates electronic excitation. Reactions of this type occur with large cross sections, and frequently have near unit efficiency for producing excited products [Vel76]. These reactions have been likened to "harpooning" reactions because the readily ionized rare gas atom can transfer its outermost electron to the halogen at a rather large distance (5-10Å), "harpooning" it and forming an ionic bond [May73]. The reactions have rate coefficients on the order of $10^{-9} \text{ cm}^3 \text{s}^{-1}$, and in typical mixtures result in lifetimes of excited Kr^{*} atoms on the order of 10 ns [Bra79]. Once the excimer is formed, it will decay via spontaneous emission and collisional deactivation giving the molecule a lifetime of ~ 2.5 ns.

Discharge Physics

The energy necessary for the generation of the excited species in the preceding reactions is pumped into the gas mixture through avalanche electric discharge excitation [Chr94]. Electron beam and nuclear pumped lasers have been examined, but electrical discharges offer the potential for higher pumping efficiency and higher average power [Bra79]. The reason for the higher efficiency is that it is possible,

with a carefully controlled discharge, to pump metastable levels of the rare gases directly by electron impact with a very high efficiency. Using the molecular lifetime given above, moderate output energies on the order of several hundred millijoules dictate a population density requirement on the order of $10^{15}/\text{cm}^3$ [Chr94]. Therefore in order for lasing to occur, the formation rate of the ionic and excited precursors must be fast enough to produce excimers at a rate of several $10^{23}/\text{cm}^3/\text{s}$. In order to achieve these formation rates certain requirements must be met. First, the fast kinetics of the gases require total gas pressured in the range of 2 to 4 atmospheres. Second, the discharge parameters need to include electron densities on the order of $10^{15}/\text{cm}^3$, current densities of $10^3 \text{ A}/\text{cm}^2$, and electron temperatures of $\sim 1200 \text{ K}$. This results in electric discharge field strengths of $10\text{-}15 \text{ kV}/\text{cm}$, leading consequently to discharge-electrode spacings of 2-3 cm.

Beam Profile

The quality of an excimer laser beam is intimately coupled to the discharge [Chr94]. A homogeneous breakdown of the gas is required for uniform output, and this is ensured typically by preionization of the gas just prior to the full-blown discharge. The preionization is provided by UV light that is created by spark gaps (using preionization pins) that

run along the length of the electrodes. Though the preionization step is effective, there is still a practical limitation on the cross-sectional dimensions of a homogeneous beam due to the strong absorption of the UV light by the laser gas.

A three-dimensional beam profile from a Lambda Physik LPX 300 KrF laser may be seen in Figure 2-1. A Lambda Physik LPX 305 excimer laser working with KrF was used in this work, so the beam profile shown may be considered applicable. The profile shown represents that of "multigas" electrodes configuration. Another configuration available is that of "fluorine-optimized" electrodes, which has a higher full-width at half-max in the vertical cross section than the "multigas" electrodes configuration.

Laser-Solid Interactions

Electromagnetic radiation with wavelength ranging from ultraviolet to infrared interacts exclusively with electrons, as atoms are too heavy to respond significantly to the high frequencies ($\nu > 10^{13}$ Hz) [All180]. Therefore, the optical properties of matter are determined by the energy states of its valence electrons (bound or free). Bound electrons generally only weakly respond to the external electromagnetic

wave and affect only its phase velocity. Free electrons, however, are able to be accelerated and therefore extract energy from the field. Since the field is periodically changing, the oscillating electrons reradiate their kinetic energy (cause of reflection) or undergo collisions with the atoms, transmitting their energy to the lattice.

Absorption of incident energy fundamentally dictates the resultant thermal state of the material and therefore is a suitable point to begin an analysis of laser-solid interactions. The complex refractive index, n' , defines two quantities which describe the degree of coupling of the incident radiation with the material, namely reflectivity R and absorption coefficient α . It is defined as [Hum85]:

$$n' = n - ik \quad (2.1)$$

where n , the real part, is the ratio of the phase velocities in vacuum and the material. The extinction coefficient k describes the damping of the light wave. For normal incidence, reflectivity and absorption are related to n and k by, respectively:

$$R = \frac{(n-1)^2 + k^2}{(n+1)^2 + k^2} \quad (2.2)$$

and

$$\alpha = \frac{4\pi k}{\lambda} \quad (2.3)$$

where λ is the wavelength of the radiation.

As mentioned previously, the mechanisms involved in absorption of incident radiation in materials are defined by the electronic structure of the material, and therefore it is useful to discuss exclusively semiconductors, as they are the focus of this work. In semiconductors, five distinct mechanisms for the absorption of light can be identified [Woo84]:

- (1) Photons with energy (hv) much less than the band-gap energy (E_g) can excite lattice vibrations directly.
- (2) Free or nearly free carriers can be excited by absorption of light with $hv < E_g$; such carriers will always be present as a result of finite temperatures and/or doping.
- (3) An induced metallic-like absorption due to free carriers generated by the laser radiation itself

can occur.

- (4) For photon energies $> E_g$ absorption will take place by direct and/or indirect (phonon-assisted) excitation of electron hole pairs.
- (5) Absorption induced by broken symmetry of the crystalline lattice is possible.

The largest contributions to absorption of laser radiation with $h\nu > E_g$ by crystalline or amorphous silicon are found in mechanisms (4) and (5), respectively. Mechanism (3), however, may be the cause of discrepancies of actual as compared to calculated absorption coefficient values [Low83]. Though the focus here is on absorption of ultra-violet radiation (KrF excimer laser operating at 248 nm) by amorphous or fine-grained polycrystalline silicon, the state of the material is not particularly critical in this instance because α is saturated at $\sim 10^6 \text{ cm}^{-1}$ for this wavelength in silicon. This value is more characteristic of metals, and is virtually independent of both temperature [Ong88] and state of the material, i.e., it is approximately the same for crystalline, amorphous, and liquid silicon. An analysis of absorption coefficient as a function of temperature by Jellison, et al.

[Jel82] reinforces this as no change in α was observed over the temperature range 300 - 1000K for 355 nm Nd:YAG radiation.

Reflectivity values for silicon are dependent on wavelength as well as crystalline state. Absorption coefficient and reflectivity values for crystalline silicon at room temperature as a function of wavelength are shown in Figure 2-2. From this figure it can be seen that the reflectivity demonstrates relatively high values in the UV regime and represent R-65% for 248 nm radiation. Though the reflectivity is relatively high in the UV regime, the absorption coefficient is at its maximum values. The optical properties of silicon are discussed in greater detail later in this chapter.

Silicon is an indirect band-gap material [Ohr92]. This means that the maxima of the valence band does not occur at the same point as the minima of the conduction band in k -space, where k is the wave vector. As mentioned previously, absorption of radiation with $h\nu \geq E_g$ predominantly occurs by interband transitions, this case including those of an indirect nature. An indirect transition requires a change in both energy and momentum (the quantity k is proportional to the momentum). A two-step process is therefore required because the photon can provide a change in energy but not (significantly) in momentum. Momentum is conserved via a

phonon interaction as illustrated in Figure 2-3. Though a phonon can only absorb very small energies, it is able to absorb a large momentum when compared to an electron [Hum85]. Also, although a broad spectrum of phonons is available, only those with the required momentum change are usable. Typically these are longitudinal and transverse-acoustic phonons [Pan71]. Direct transitions are also possible in an indirect gap material, if the photon energy is sufficient ($h\nu > 3.4$ eV for Si). This explains in part the high absorption coefficient values observed for UV radiation ($h\nu \sim 5$ eV).

When a beam of photons of energy $h\nu > E_g$ is absorbed in a semiconductor, excited carriers are generated [All80]. Relaxation of the hot carriers, which results in lattice heating [Rea71], is a complex process and an area of active research [Kur87]. Excited carrier relaxation times on the order of picoseconds have been derived and confirmed using time-resolved investigation of the absorption coefficient. As incident radiation is converted to increasing lattice temperatures, the thermophysical properties of the material dictate temperature distribution and phase changes. This aspect of laser annealing area has been actively investigated [Cul82, Dev85, Gal85, Gri93, Ish95] and is discussed in greater detail later in this chapter.

Silicon Thin Film Technology

Polycrystalline silicon (poly-Si) thin films have been a key material in silicon integrated-circuit technology since the poly-Si gate metal-oxide-semiconductor very large-scale integration (MOS VLSI) technology was developed in the mid 1970's [Kam88]. Polycrystalline silicon can be used as a semiconductor in field-effect devices. By fabricating active devices in poly-Si thin films, numerous novel applications are feasible. This is because the devices can be built on poly-Si that has been deposited on transparent and insulating substrates which can be much larger than the silicon wafers available [Yam94].

One of the major hurdles in the use of poly-Si thin films as a semiconductor in active devices on insulating substrates is the processing-temperature limitation of the inexpensive glass substrates such as Corning 7059, which has a quoted working range below 600°C [Bac90]. The resultant grain size of the poly-Si films that are deposited on these glass substrates, by such common methods as low-pressure chemical-vapor deposition (LPCVD) and sputtering, are relatively small (~0.05 μm or less [Kam88]) and result in poor material quality. Carrier mobilities of poly-Si (TFTs) using such as-deposited films are $\leq 10 \text{ cm}^2/\text{V}\cdot\text{s}$ for *n* channel devices [Hat87].

Applications

One of the most important applications of poly-Si TFTs is active matrix liquid crystal displays (LCDs) in which a TFT is placed at each picture element, or pixel [Tsu93]. The TFT switch charges and discharges the liquid-crystal cell's transparent electrodes thereby turning the pixel on and off. Active addressing can be used to overcome two of the main problems with direct-multiplexed liquid-crystal displays (i) decrease in contrast and (ii) narrowing of viewing angle as the number of lines increases. This is because the charge on the pixel electrodes can be stored by using the TFT at the pixel which works as a nonlinear active element [Yam94].

Some consumer applications of the active-matrix liquid crystal displays include direct-view displays for laptop computers [Haj94], light-shutter based projection displays, and small displays such as video camera viewfinders [Yam94]. Amorphous silicon TFTs have been used for large direct-view displays [Tsu93] even though the field effect mobilities are around $0.5 \text{ cm}^2/\text{V}\cdot\text{s}$. The ease of fabrication and low maximum-temperature processing make this approach attractive. However, a particularly important advantage that poly-Si TFTs have over amorphous TFTs is that integrated peripheral circuits as well as the active-matrix can be fabricated on the same glass substrate [Ser89]. In TFT LCD configurations,

there is a grid of gate buslines and data buslines that have TFTs at each intersection. The number of lines that must be connected to peripheral circuits is the sum of the data and gate buslines. Therefore, as resolution is increased, assembly becomes much more complicated. Integrated peripheral circuitry can reduce this to simple lithographic steps, reducing assembly and manufacturing cost. This integrated peripheral circuit scheme has been fabricated and proven technologically feasible [Tak91]. Regarding light-shutter projection devices and small displays, poly-Si TFTs are much more suitable than amorphous Si TFTs. In order to achieve the large effective pixel area necessary for these devices, high mobilities are necessary and can only be attained through poly-Si TFT technology.

Another important application of poly-Si TFTs is contact imagers [Yam93]. A cross section of a two-dimensional contact image sensor is shown in Figure 2-4. The contact sensor has no lens system, and the equipment size can be minimized. Some of the current image-sensing technology takes advantage of an amorphous silicon photodiode formed on a glass substrate used as a light detector. However, to send out the detected signals rapidly enough, the read-out circuits should be incorporated onto the same substrate. Successful integration of poly-Si TFT circuits such as shift registers with a one-dimensional array of amorphous silicon photodiodes has been

achieved [Kan91].

New applications for poly-Si TFTs may be found in thin-film electroluminescent (TFEL) displays and electro-optic devices for optical interconnections [Yam94]. TFEL display technology is currently limited by the dimness of the red and blue colors in direct-multiplexed displays. Active-matrix addressing can be used to overcome the dimness problem, though consideration must be given to other problems, such as high drain-to-source breakdown voltage of TFTs [Ung84]. However, an active-matrix TFEL display has been successfully fabricated using amorphous silicon TFTs [Sak92]. Given the improved electrical characteristics of poly-Si TFTs, an improvement in drive frequency would be possible using the poly-Si technology.

Optical interconnection technology is being studied intensively, and one of the challenges in the field involves free-space optical switching. A 1024-input-port optical switching module has been developed [Shi92] using liquid-crystal-cell array addressed by a poly-Si TFT active matrix combined with a birefringent plate. The liquid-crystal material may ultimately be replaced with a ferroelectric liquid crystal which has a switching time of ~50 μ s, which is three orders of magnitude faster than the twisted-nematic liquid crystals currently used in flat-panel displays. Fast addressing will require the high mobility of poly-Si TFTs.

Thin Film Transistor (TFT) Structure

An important feature of TFTs is that they can be built on transparent insulating substrates such as glass or fused quartz, thereby allowing optical transparency of the device structure. This also allows use of larger substrates than possible with silicon wafers. A schematic cross-section of three common types of silicon TFT structures may be seen in Figure 2-5. The structure is similar to that used in metal-oxide semiconductor field-effect transistor (MOSFET) technology, consisting of a source, drain, and gate. A potential is applied between the gate and the source, increasing the number of carriers beneath the gate region to make the area more conductive. Carriers may now flow from the source to the drain, producing an amplified signal [Ask89]. By changing the input voltage between the gate and the source, the number of carriers in the conductive path changes, thus changing the output signal.

Effects of Microstructure on TFTs

Though poly-Si films have been widely used as passive devices in integrated circuits, the conduction properties are poor [Sag89]. Many reports [Im94, Sag89, Dye93, Kur93, Mor89, Nar84] center around the effects of grain size on electrical properties, though there is not a direct relationship of the grain size with carrier mobility (see TFT Processing

Techniques subsection). The highest field-effect mobility shown by any of the commonly used processing techniques is crystallization of a-Si with an argon laser. This technique exhibited mobility of $390 \text{ cm}^2/\text{V}\cdot\text{s}$ although the grain size of the crystallites is only $0.05 \mu\text{m}$ [Shi92]. An analysis of the intra-grain structure as a function of annealing technique is therefore necessary in order to ascertain the effects of lattice defects on mobility. Also, it is necessary to examine the effects of grain boundaries residing within the channel of the transistors on the overall device performance.

A study by Haji et al. [Haj94], focuses on the morphology and the type of defects on a-Si films annealed by conventional furnace and by rapid thermal processing (RTP) using transmission electron microscopy (TEM). They used a-Si samples deposited at 550°C by LPCVD method on glass. The films were then annealed in either a conventional oven at 600°C for several hours or were subjected to RTP at temperatures ranging from 650 to 850°C for several minutes. Their study also included an in-situ anneal in the TEM by using the TEM's heating stage. This allowed observation of grain growth reorganization of microstructure. In their analysis they found the following: Crystallization of a-Si in a conventional oven or by RTP solely proceeds through the formation of microtwins. The twins permit a high rate of growth in two dimensions, which results in crystallites with

an ellipsoidal form. The main defects inside grains are therefore twins and while first order twins are electrically inactive, their presence is commonly related to: (i) incoherent {112} steps perpendicular to {111} twin planes which introduce dislocations at the step edges which are strongly electrically active, and (ii) higher order twins which are related to displacement vectors and are electrically active due to segregation of dissolved impurities.

Microstructures in laser annealed films result from a vastly different process than conventional furnace or RTP annealing techniques. The a-Si films are completely melted by the laser therefore the microstructure of the solidified films is not a product of solid-state nucleation and growth but rather a kinetic process, details of which are discussed later in this chapter. A comparison of the microstructures resulting from furnace anneal, RTP, and laser anneals done previously [Via94] discusses the disparity between electrical properties resulting from each process. The density of intra-grain defects was examined using plan-view TEM and it was found to be much higher in the solid-phase annealed films. The lower mobility values observed in RTP and furnace-crystallized films as compared to films solidified from melt in laser annealing were attributed to the morphological differences. The intra-grain defect structures occur substantially less frequently in laser-annealed films as

compared to solid-phase annealed films.

As mentioned, the effect of grain boundaries residing within the channel of the transistors on overall device performance is a critical issue. The presence of the grain boundaries complicates the operation mechanisms of the polysilicon TFTs, as compared to their single-crystal counterparts [Dim93], because the grain boundaries act as charge traps which lower the effective carrier mobility and increase the threshold voltage of the TFT. Potential solutions to this problem include passivation of the grain boundaries with hydrogen [Fau89]. The hydrogen terminates the non-tetrahedrally coordinated ("dangling bond") silicon atoms and prevents the creation of the most effective recombination site [Sea79]. This passivation step can be accomplished by diffusing hydrogen directly from a gas by using a deposited silicon nitride layer as a diffusion source, or by hydrogen implantation with a silicon nitride capping layer. The results of these techniques showed a systematic shift in transistor leakage current for both n-channel and p-channel devices as a function of the degree of hydrogen passivation. With respect to laser annealing, however, the hydrogenation process is less than adequate because explosive effusion of hydrogen occurs in the melting phase of the pre-hydrogenated film and, if a post-anneal hydrogenation process is attempted, difficulties are encountered due to overlayers. Also, long

diffusion times are necessary for hydrogen to go from the contact holes to the center of the channel [Cho94].

Another solution includes reduction of size in the channel of the TFT [Yam91]. The improved characteristics of the TFTs with the small channel dimensions may be related to the decrease in the absolute number of grain boundaries in the active channel of the device. Figure 2-6 depicts schematically the distribution of grain boundaries in the large-grain TFT with large channel dimensions and one with small dimensions, assuming a grain size of $\sim 1 \mu\text{m}$. In the case of the small-dimension TFT, very few grain boundaries are located in the channel region resulting in reduced leakage current and improved threshold voltage and carrier mobility.

Both of the solutions mentioned above are useful in reducing the magnitude of the problem, but modeling of the TFTs is still difficult. King et al. [Kin94] use an "effective-medium" approach in which the effects of grain-boundary defects and intragranular defects are assumed to be uniformly distributed. The trap states that are associated with these defects are taken into account using an effective density-of-states distribution within the silicon band gap. Their results showed that effective density-of-states distributions cannot be assumed to be symmetric about the Fermi level and cannot be approximated by a generic sum of exponential-tail distributions. Conclusively, though the

techniques mentioned above for solving microstructually-induced difficulties have shown potential for achieving high transconductances, modeling the TFTs is complex and a technology to control the grain boundary location may be essential to make practical applications feasible [Yam91].

TFT Processing Techniques

Techniques that have been investigated for the formation of TFTs include the use of as-deposited amorphous films or these same films followed by furnace anneal, ion implantation then furnace anneal, rapid thermal processing, and laser annealing. The carrier mobilities related to each process are

1. As-deposited amorphous films: $\sim 1 \text{ cm}^2/\text{V}\cdot\text{s}$ [Yam94]
2. Furnace anneal: $10-50 \text{ cm}^2/\text{V}\cdot\text{s}$ [Bon91]
3. Rapid thermal processing: $10-50 \text{ cm}^2/\text{V}\cdot\text{s}$ [Kak89]
4. Laser annealing: $200-300 \text{ cm}^2/\text{V}\cdot\text{s}$ [Ser89]

Carrier mobility does not seem to depend solely on grain size, however, as the high mobilities associated with the laser annealing process coincide with grain sizes ($\sim 150 \text{ nm}$) that are smaller than rapid thermal processing ($\sim 250 \text{ nm}$) or furnace annealing ($\sim 1000 \text{ nm}$). Some of the morphological reasons for this are examined in the discussion section.

Currently, there are three techniques that result in poly-Si films with a carrier mobility greater than $50 \text{ cm}^2/\text{V}\cdot\text{s}$ [Yam94]. They are (1) solid-phase recrystallization of low-pressure chemical-vapor deposited (LPCVD) thin films [Nak91], (2) solid-phase recrystallization using a combination of self-implantation and thermal annealing [Ive87, Kum94, Nom91, Ive85], and (3) laser annealing of polycrystalline or amorphous silicon thin films [Bac90, Sam89, Ser89a, Ser89b]. To date, laser annealing has resulted in the highest carrier mobilities, including $383 \text{ cm}^2/\text{V}\cdot\text{s}$ and $400 \text{ cm}^2/\text{V}\cdot\text{s}$ [Sel94].

Much work has been done in the area of solid-phase recrystallization of LPCVD silicon thin films deposited on low-cost glass substrates for use in TFT technology [Haj94, Sag89, Ols85, Sak91, Nak91]. Though the maximum mobility attained has not been the highest with this technique, there is still significant interest because, if a viable technique were to be developed that used common furnace configurations, the upstart costs would be minimized. Research in the area has included recrystallization mechanisms [Ols85, Haj94], deposition-gas effects [Nak91], and film-substrate interface effects [Sak91].

Solid-phase recrystallization using a combination of self-implantation and thermal annealing is a technique that aims at controlling the nucleation density before the final

anneal in order to get large grain structures. The process is as follows [Nom91]. Silicon films are formed on glass or quartz substrates by LPCVD at some temperature that is within the working range of the substrate, typically $< 600^{\circ}\text{C}$. Films of this nature typically have grain sizes below 50 nm, depending on the deposition temperature. The films are then amorphized by Si^+ ion bombardment with energy ranging 20-100 KeV and doses of $\sim 1 \times 10^{15}$ ions/cm² [Kum94]. Then the final anneal, typically $\sim 600^{\circ}\text{C}$, is performed. Resultant grain sizes using this technique are relatively large (1-2 μm) and carrier mobilities are high (10-100 cm²/V•s) [Yam94].

The theory behind this technique is that the ion implantation step inhibits nucleation by amorphizing the majority of the film. The subsequent anneal provides sufficient thermal activation for grain growth but not for extensive continued nucleation, allowing the remaining nucleated clusters to grow without being impeded by competing clusters. Kumoni et al. [Kum94] investigated the nucleation kinetics involved in this process and concluded that suppression of the nucleation is most effective when the ion energy exceeds a value at which the projected range of the ion reaches the interface of the underlying film. This led them to conclude that nucleation occurred at the interface, as opposed to potential homogeneous nucleation.

Laser annealing of polycrystalline or amorphous silicon

thin films is the third technique investigated for TFTs and is discussed in detail in the next section of this chapter.

Laser Crystallization of Silicon Thin Films

Since the first results related to laser annealing of ion-implanted semiconductors were obtained, the number of published papers in the field has increased enormously [Boy95, Bro93, Cho95, Gal81, Gro93, Nar84, Woo81]. As mentioned previously, laser crystallization of poly-Si films results in the highest carrier mobility attained by any technique. However, although investigations on this technique have been actively performed [Im93], the precise transformation mechanisms are not yet well understood. Also, attempts at quantitative estimates of the effects of high-power laser irradiation have been limited due to the lack of precise temperature and phase-dependent optical and thermophysical parameters [Ong88]. A literature review of the currently available data on this topic follows.

Optical and Thermophysical Properties of Silicon

The optical and thermophysical properties of amorphous silicon films are critical aspects regarding laser crystallization because they dictate the material response to the incident radiation. To begin, the optical properties of

amorphous silicon (a-Si) are sensitive to preparation conditions and doping with hydrogen [Pil85]. The amount of disorder in the samples is determined by substrate temperature, deposition rate, deposition method, impurities, and vacuum conditions. Another factor affecting the films is the mismatch of thermal expansion coefficients of the sample and substrate, which can cause grain boundaries and voids in the samples. Conclusively, the actual morphology and ensuing properties of an amorphous sample depends on method of preparation and its particular thermal history [Wil95].

Extensive research has been done on the optical properties of silicon [Bro70, Buc94, Cab91, Fri92, Kun91, Pil85, Sir79]. Absorption coefficients have been measured for many wavelengths and preparation techniques. As mentioned earlier, the absorption coefficient of amorphous silicon for UV radiation is high (10^6 cm^{-1}). This values is consistent with others in the literature: $1.5 \times 10^6 \text{ cm}^{-1}$ [Una89], $1.4 \times 10^6 \text{ cm}^{-1}$ [Ong88]. Reflectivity measurements of amorphous silicon at 248 nm wavelength are also consistent. Piller [Pal85] gives values of $R \sim 0.55$. Other values include: 0.55 [Una89], and 0.54 [Ong88].

The absorption coefficient values given above can be compared to the characteristic thermal diffusion length, $(2Dt)^{1/2}$ [Poa82], to ascertain relative importance of absorption and thermal properties. The heat diffusivity, D ,

(~ 0.5 cm²/s) and τ is the pulse length (~ 2.5x10⁻⁸ s), giving a characteristic thermal diffusion length of ~ 1.6 μ m. The absorption length of the beam within the sample surface is therefore much shorter than the thermal diffusion length during the pulse. This implies that a detailed knowledge of the temperature-dependent thermal conductivity may be more important in order to describe the processes occurring.

From consideration of simple kinetic theory, the thermal conductivity κ can be expressed as [Ong88]

$$\kappa = \frac{1}{3} c_v l u \quad (2.4)$$

where C_v is the specific heat (due to the phonons) per unit volume, u is the phonon velocity and l is the mean free path of the phonons. Though the scattering mechanisms of the phonons contributing to the value of l are well known for crystalline silicon (c-Si), they are not clearly understood for amorphous silicon (a-Si). Due to the disordered structure in a-Si and thus stronger phonon scattering probability, the value of thermal conductivity is much lower. Incorporating an approach used with other amorphous materials, Ong et al. [Ong88] proposed the following expression:

$$\kappa(T) = 4.8 \times 10^{-9} (T-900)^2 + 3.7 \times 10^{-6} (T-900) + 3.7 \times 10^{-2} \frac{W}{cm K} \quad (2.5)$$

which describes the thermal conductivity as a function of temperature from 300-1420 K. The reason that this temperature range is given is related to the widely accepted [Una89] melting point of a-Si given as 1420 K.

The other thermophysical property of interest is the specific heat capacity, C_s . This is also often given as a temperature dependent term, increasing the accuracy of any model choosing to incorporate such data. One detailed function is given as [Fog93]

$$C_s(T) = -0.69 \exp (2.375 \times 10^{-3}T) - 8 \times 10^{-3} \times 1 \times 10^{-4}T \quad (2.6)$$

for $T > 300$ K.

Mechanisms in Pulsed Laser Crystallization

During pulsed laser crystallization of amorphous silicon thin films, the incident radiation leads to surface melting when sufficient energy is used. This liquid phase becomes unstable as cooling takes place after the pulse is over. The mechanisms (nucleation and solidification) that then take place and lead to the resultant microstructure have been actively investigated [Boh96, Im93, Win90, Cho94, Sam93, Nar85].

Nucleation and solidification processes in pulsed laser crystallization of silicon thin films can be broken down into

two regimes, differentiated by whether complete melting of the film occurs.

In the first case, where complete melting of the film does not occur, several potential scenarios have been proposed. Thompson et al. [Tho84] and Lowndes et al. [Low84] both support the following dynamic. At low energy densities the laser energy only melts a portion of the film, creating a thin liquid layer near the surface. As the liquid begins to solidify as relatively large-grain polycrystalline silicon, the latent heat released raises the temperature of the resolidified poly-Si above the temperature of the first-order phase transition of a-Si to the metallic liquid, T_{a-1} . The underlying a-Si material then begins to melt. This new liquid is severely undercooled compared to the poly-Si layer and therefore resolidifies as fine-grained poly-Si. Thus a thin liquid layer is presumed to propagate through the a-Si material as a result of the released latent energy. This is the explosive recrystallization process and is shown schematically in Figure 2-7. It is self-sustaining until eventually it is quenched by the energy required to raise the temperature of the a-Si solid in front of the liquid to T_{a-1} .

The final microstructure consists of a top layer of large-grained (50-100 nm) polycrystalline silicon with a layer of fine-grained (1-10 nm) poly-Si directly below it resulting from the explosive recrystallization process. Thompson et al.

[Tho84] were able to support the explosive crystallization argument by use of transient reflectance and conductance measurements. Even though the reflectivity returns to the solid value at ~ 53 ns, the conductance showed a second peak that existed for an additional 10 ns (until ~ 63 ns) and was attributed to the subsurface liquid layer which behaves as a metallic conductor. Using this information they were also able to estimate the velocity of the explosive melt front between 10 and 20 m/s.

The other proposed scenario for non-complete melting of Si films is by Im et al. [Im93]. Im argues that in his films explosive crystallization of a-Si occurs at the onset of the transformation, implying that partial melting of explosively crystallized fine-grained Si is occurring rather than partial melting of an amorphous film. It is suggested that early triggering of explosive crystallization may be attributed either to (i) the presence of microcrystalline clusters in the LPCVD samples, which was confirmed by analyzing solid-phase crystallization behavior and is absent in high-dose ion irradiated amorphized samples and/or (ii) the possible presence of impurities, such as hydrogen.

The same researchers also put forth the idea of the Super Lateral Growth (SLG) regime. In this regime, almost complete melting of the film occurs to the extent that there is a discontinuous Si film composed of discrete islands. Growth

from these clusters proceeds, resulting in an unusually large (300-400 nm) grain size. If greater laser energy is used the resultant grain size returns to smaller values (~50-100 nm), typical of lower-energy density irradiation as mentioned above.

In the second case, where complete melting of the film does occur, there is substantial evidence that nucleation occurs homogeneously. Stiffler et al. [Sti91, Sti88] argue the following. They used 200 to 400 nm-thick Si films that were deposited on SiO_2 layers that varied between 77 and 330 nm. The Si films were melted using a Q-switched ruby laser (25-30 ns pulses) and transient conductance and reflectance measurements were performed *in situ*, as shown in Figure 2-8. Analysis of the measurements reveal the following scenario. After melting in the first 10-20 ns, the film remains fully molten as it cools with conduction to the substrate (Region I). Nucleation of the crystalline phase initiates rapid solidification and is indicated by a change in reflectance and conductance values. Nucleation is followed by rapid solidification, which is indicated by a fast (~10 ns) drop in the reflectance and conductance (Region II), as the enthalpy released heats the film to the steady-state solidification temperature determined by the thermal properties of the substrate. Recalescence is followed by steady state

solidification which is marked by a gradual (150 ns) decrease in conductance returning to the solid value (Region III).

Undercooling of the films was calculated in the following manner. They determined the volume fraction of solid following recalescence from the ratio of the conductance to the fully liquid value assuming a two phase mixture and relative conductivities. The volume fraction of liquid consumed during recalescence was then used to determine the temperature of the liquid prior to nucleation using a heat balance equation. Since the heat loss to the substrate is exactly balanced by the release of enthalpy in the film during steady-state solidification, the thermal flux out of the film following recalescence was obtained from the slope of the conductance trace. This thermal flux can be used to establish an upper limit for the quench rate of the film prior to nucleation by using the specific heat and thickness of the film, and also can define an upper limit for the thermal leakage during recalescence. Also, T_{ss} , the steady-state solidification temperature, can be estimated from the thermal flux. This is done by calculating an effective interface velocity from the thermal flux and enthalpy of melting, which is then used to calculate T_{ss} . From the quench rate, the supercooling can be calculated. Supercooling prior to nucleation was constant and ~500 K for quench rates below $\sim 10^{10}$ K/s.

As in previous studies, no evidence of preferential nucleation at either the surface or interface was present. The microstructure consisted of coarse grains combined with interspersed fine grained structures, which typically are the signature of explosive recrystallization. This morphological idea is further reinforced in the most recent work by Im et al. [Im94] in which they found the SLG regime to result in large single-crystal disk structures as shown in Figure 2-9. They argue that these disk structures are the result of a single nucleation event occurring from a discreet cluster that was not melted in the near-complete melting of the film. These disk structures are predicted to occur when the separation distance between surviving solid clusters is greater than the maximum lateral growth distance. In other words, as the single crystal disks are growing there is significant supercooling of the liquid which leads to nucleation of solids in the bulk of the liquid ahead of the advancing solidification front, which stalls the growth of the grains and results in the morphology shown. A variation on this morphology was also observed in which the seeds that survive are located in close proximity to each other such that growth can continue until the solidification fronts of neighboring disks touch. This results in single crystal disks touching with small regions of fine poly-Si grains in between the disks.

Previous Work

To provide perspective to the results outlined in this work, the conclusions of two sets of experiments previously done by the author are presented. The first set focused on examining the effect of a 500 Å-thick SiO_2 capping layer on the microstructure of amorphous silicon thin films crystallized using various techniques. Samples with and without this capping layer were annealed using a conventional furnace, rapid thermal annealing (RTA), and an excimer laser.

The resultant microstructures were examined using transmission electron microscopy (TEM). It was expected that the capping layer would have varying effects on the resultant microstructure, depending on the annealing technique. For furnace and rapid thermal annealing, nucleation would be affected due to the addition of a new interface. The microstructure could also be affected due to changes in conductive and radiative losses during processing. For RTA, it was expected that there would be other effects due to storage of thermal energy in the capping layer. In laser annealing, there would be surface reflectivity effects as well as thermal effects due to changes in thermal gradients, as well as heat flow, during processing.

The objective in the second set of experiments was to

examine the effect of varying the thermal quenching in a laser-annealed film. The quench rate of a molten surface film is determined by thermal flux to the substrate and the thermal capacity of the film. Computer simulations have shown that for substrate configurations in these experiments (SiO_2 on Si wafer) heat transfer is strongly dependent on the thickness of the SiO_2 layer [Sti91]. Therefore, the thermal flux out of the amorphous thin film can be varied by changing the thickness of the underlying oxide layer. Changing the thermal flux would affect undercooling and nucleation kinetics and therefore resultant microstructure. Consequently, samples with intermediate oxide layers of varying thickness were laser-annealed using various energy densities, and the resultant microstructures were examined using plan-view and cross-sectional TEM.

Three types of samples were used in the experiments. For the comparison of anneal techniques, two sets of samples were used. These samples were prepared on (100) silicon with an initial 200 Å-thick thermal oxide grown at 1000°C using wet oxidation. An 800 Å-thick amorphous silicon layer was deposited at 555°C in an LPCVD furnace using silane chemistry. One set of samples had a 500 Å-thick capping layer of SiO_2 that was plasma deposited by decomposition of tetraethylorthosilicate (TEOS) at a temperature of 450°C. The low-temperature based capping layer is provided to promote

uniform grain growth as the recrystallization mechanisms begin. The second set of samples consisted of the wafer, thermal oxide, amorphous silicon layer, and an 80 Å-thick oxide layer on top.

The third set of samples, which were used exclusively in the laser-based experiments, consisted of a 1000 Å amorphous silicon film deposited on an SiO_2 layer using LPCVD at 550°C. The intermediate oxide layer varied in thickness (400, 1200, 2200 Å) and was deposited on a (100) silicon wafer using wet oxidation. Samples that were subsequently characterized for carrier mobility were doped with boron at $5 \times 10^{18} \text{ cm}^{-3}$.

The annealing step for each technique was done as follows. Laser annealing was performed with a KrF excimer laser operating at a wavelength of 248 nm, using energy densities from 190 to 505 mJ/cm^2 . The samples were processed in air at room temperature. Single laser pulses were used for the undoped samples, while a beam scan was performed on the doped samples in order to crystallize an area of sufficient size for electrical characterization. It has been reported that increasing the number of pulses does not show any further grain growth [Bac90], and this was reinforced by our results as there was no significant deviation in resultant grain size in the scanned versus non-scanned samples.

Rapid thermal processing was done with the AG Associates Heatpulse 8108 using ramp-up and ramp-down rates of 70°C/s

with a plateau of 1050°C for 30 seconds. Furnace anneals were performed at 600°C for 24 hours in a conventional furnace.

Bright-field plan-view TEM was used to analyze the resultant microstructure of the samples. Micrographs representing each of the thermal treatments are shown in Figures 2-10 - 2-12 for uncapped samples. The most notable difference in microstructure occurs between the laser-annealed samples and the solid-phase annealed samples. For RTA and furnace anneals, the microstructure consists of relatively large but poorly-defined grains which have a high intragrain defect density. A high density of twins is also observed. The grains have a wide distribution of shapes and sizes, with some grains having a high aspect ratio. For laser annealing, the microstructure shows clearly-defined grains that are smaller than those of the solid-phase anneals, but with low intragrain defect density. Also, twins are not as readily observed and the grains are comparatively equiaxed. Microstructural differences are attributed to the variation in nucleation and growth mechanisms between the annealing techniques, and these differences are discussed in detail later in this work.

For experiments involving capped samples, micrographs representing each of the thermal treatments are shown in Figures 2-13 - 2-15. The microstructure of the samples was similar to that observed in the uncapped samples. One

discernable difference, however, was the average grain size. The average grain size for the various annealing techniques is shown in Figure 2-16 for samples with a capping layer and in Figure 2-17 for samples without a capping layer. The furnace-annealed samples had the largest grain size and this value did not vary significantly between capped and uncapped samples (202-204 nm). The lack of a difference in grain size between samples is due to the long processing time involved. Thermal equilibration occurs on a much shorter time scale than the 24 hour time period over which the anneal took place, and therefore the capping layer does not have any discernible effect.

The RTA samples had a smaller grain size than the furnace-annealed samples and there was a significant size difference between the capped (142 nm) and uncapped (116 nm) samples. This size difference is likely due to an increase in thermal energy stored in the multi-layer structure, as well as differences in emissivity. Enhanced containment of thermal energy in the film may be occurring from a radiative, as well as a conductive, considerations in the capped samples. Though the SiO_2 capping layer does not directly absorb significant amounts of energy from the RTA lamps, it does absorb thermal energy by conduction from the underlying Si layer. This well of thermal energy allows the growth process to continue in the underlying film even after the ramp-down step is over.

Without the capping layer, thermal energy is more quickly equilibrated since the underlying single-crystal Si wafer has a high thermal conductivity and only a 200Å SiO₂ layer is separating it from the amorphous Si layer. Also, larger radiative losses occur during processing in the uncapped samples, decreasing the amount of thermal energy available for grain growth.

The laser-annealed samples possessed the smallest average grain size. The samples processed at 190 mJ/cm² appeared to be below the recrystallization threshold, and similar results are found in other work [Bac90]. Above this energy density the resultant grain sizes ranged from 80 to 125 nm, as shown in Figure 2-18. The samples without a capping layer consistently demonstrated larger grain sizes than those with one, likely due to energy loss from the melted film to the capping layer. The SiO₂ capping layer does not absorb significant laser energy but does provide conductive losses, and therefore some quenching effect, to the underlying film. Unlike RTA, the capping layer in this situation does not provide any significant thermal storage for enhanced grain growth. The energy absorbed in the amorphous Si layer induces melting, resulting in radical temperature gradients (~ 10° K/s) [Sti91], which are equilibrated in the fashion outlined in the previous section.

Hall-effect measurements [Gha83] performed on the doped

laser-annealed samples resulted in measured mobilities that ranged from 198 to 351 $\text{cm}^2 \text{ V}^{-1} \text{ s}^{-1}$. Though the grain sizes of the laser-annealed samples were small in comparison to the other techniques, the mobilities approached that of p-type doped single-crystal silicon ($\sim 450 \text{ cm}^2 \text{ V}^{-1} \text{ s}^{-1}$). The reason for such high mobility values may be found in an examination of the intra-grain morphology. Grain boundaries, along with linear and planar defects, act as recombination centers in silicon films. Details given earlier in the "Effects of Microstructure on TFTs" subsection outlined the mode of growth of silicon films during solid-phase crystallization, including the formation of the electrically active defects. Defects of this type are not present in laser-annealed films since the final microstructure is resulting from a molten phase, resulting in the mobility values observed.

Experiments using laser annealing of samples with an intermediate oxide layer of varying thickness resulted in a microstructure with measured grain sizes between 60-200 nm. Cross-sectional TEM micrographs of the samples are shown in Figures 2-19 - 2-21. The intermediate oxide layer is visible, as well as the microstructure of the annealed Si layer. The grain boundaries are perpendicular to the plane of the film, due to the direction of heat flow during solidification. Trends of increasing grain size with laser energy were observed, as shown in Figure 2-22, with the largest grain

sizes corresponding to films which had the thickest intermediate oxide layers. Due to the relatively low thermal conductivity of SiO_2 , the oxide film's thickness becomes the major controlling factor regarding melt lifetime and nucleation and growth kinetics.

Grain-size differences between samples with 220 nm and 120 nm-thick oxide layers are less (20 nm) than those between the 120 nm and 40 nm-thick oxide layers (50 nm), suggesting that the thermal quenching effects of the oxide layer diminish with increasing thickness. Solidification velocity calculations [Via94] based on this film configuration have shown that as the oxide layer is increased in thickness there is a decrease in solidification velocity, with an asymptotic limit of 160 cm/s at a large oxide-layer thickness. This would indicate that increasing the grain size by altering thermal properties of the oxide is maximized at a certain thickness, and that value is approximately 200 nm. An oxide layer thinner than this provides greater quenching and greater undercooling of the film. As the undercooling is increased, nucleation density increases and a smaller resultant grain size follows. For the thicker oxides, the quench rate is decreased and with it the amount of undercooling. A low nucleation density ensues and there remains sufficient thermal energy in the film to allow more significant grain growth, resulting in the larger average grain size observed.

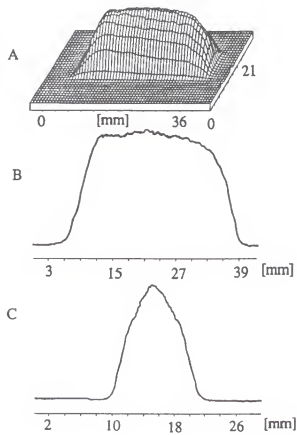


Figure 2-1 Beam profile from a Lambda Physik LPX 300 KrF laser [Chr94].

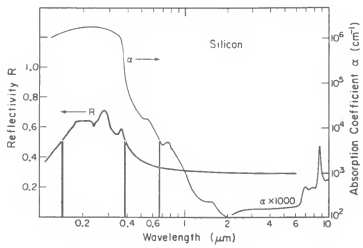


Figure 2-2 Reflectivity and absorption coefficient values as a function of wavelength for crystalline silicon at room temperature [All80].

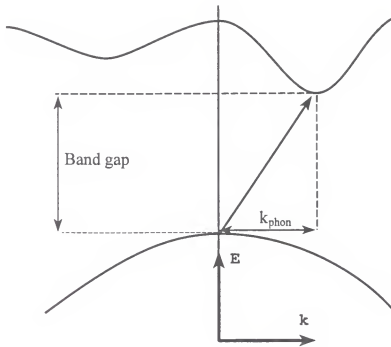


Figure 2-3 Schematic of indirect interband transition in silicon including phonon momentum exchange [Hum85].

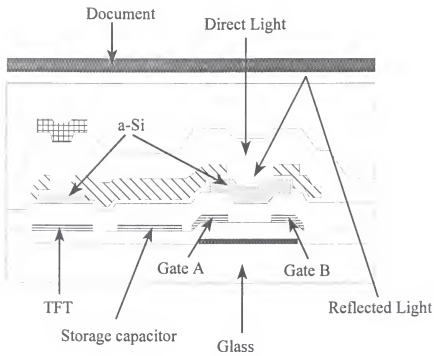


Figure 2-4 Cross-sectional schematic of two-dimensional contact image sensor [Yam93].

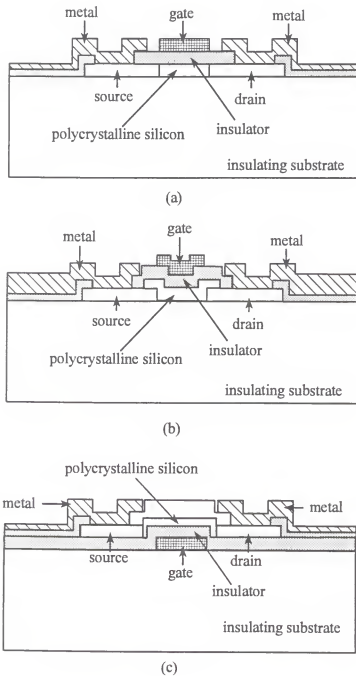


Figure 2-5 Schematic of three common types of silicon TFT structures: (a) coplanar type; (b) staggered type; and (c) inverted staggered type [Yam94].

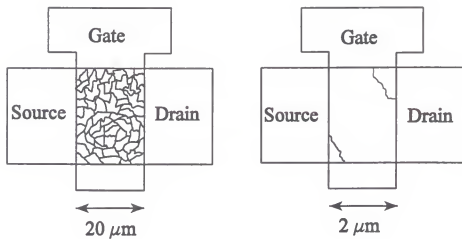


Figure 2-6 Distribution of grain boundaries in channel region in large and small TFTs.

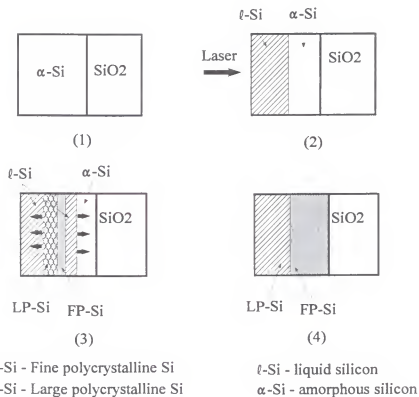


Figure 2-7 Schematic of explosive crystallization process.

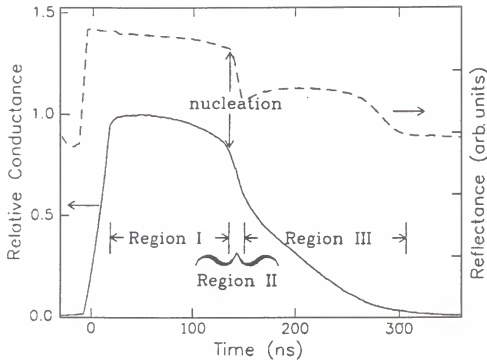


Figure 2-8 Transient conductance and reflectance measurements [Sti88].

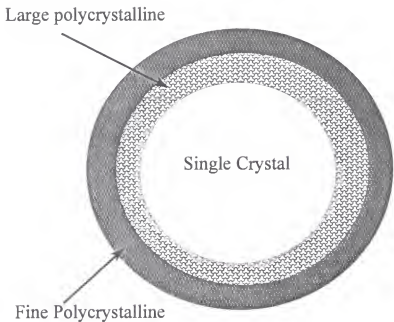


Figure 2-9 Schematic of disk structure resulting from SLG regime.



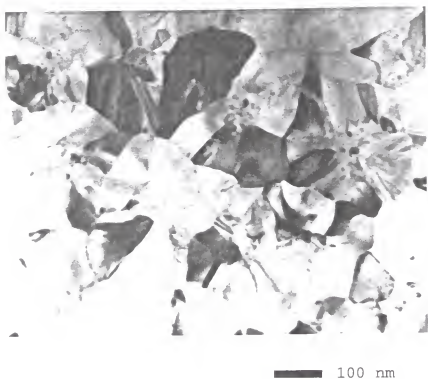
200 nm

Figure 2-10 Bright field plan-view TEM micrograph of uncapped sample annealed using furnace annealing.



100 nm

Figure 2-11 Bright field plan-view TEM micrograph of uncapped sample annealed using RTA.

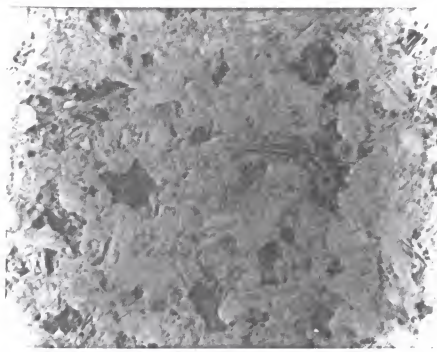


100 nm

Figure 2-12 Bright field plan-view TEM micrograph of uncapped sample annealed using laser annealing.



Figure 2-13 Bright field plan-view TEM micrograph of capped sample annealed using furnace annealing.



— 200 nm

Figure 2-14 Bright field plan-view TEM micrograph of capped sample annealed using RTA.



Figure 2-15 Bright field plan-view TEM micrograph of capped sample annealed using laser annealing.

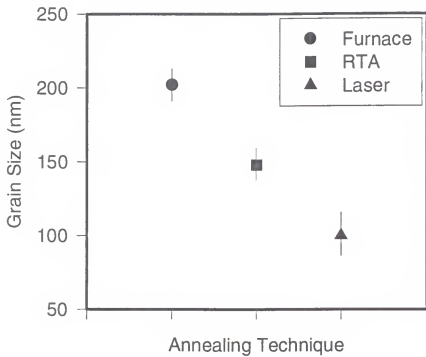


Figure 2-16 Grain size as a function of annealing technique for capped samples.

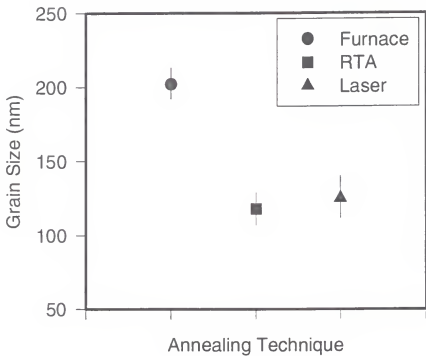


Figure 2-17 Grain size as a function of annealing technique for uncapped samples.

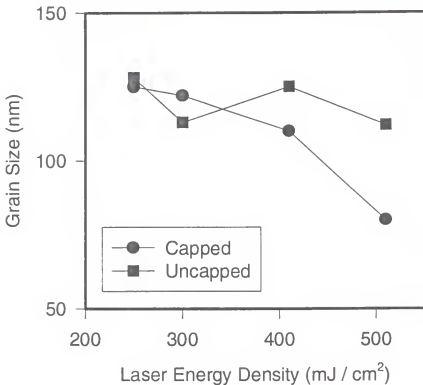


Figure 2-18 Grain size as a function of energy density for laser-annealed samples.

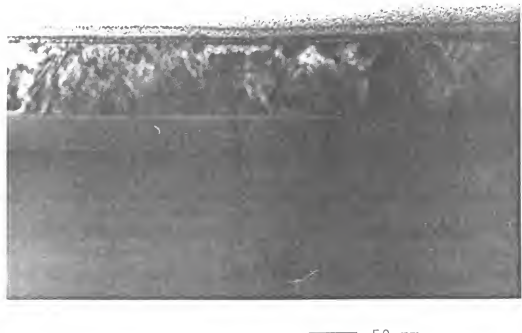


Figure 2-19 Bright field cross-sectional TEM micrograph of laser-annealed sample with intermediate 40 nm-thick oxide layer.



Figure 2-20 Bright field cross-sectional TEM micrograph of laser-annealed sample with intermediate 120 nm-thick oxide layer.

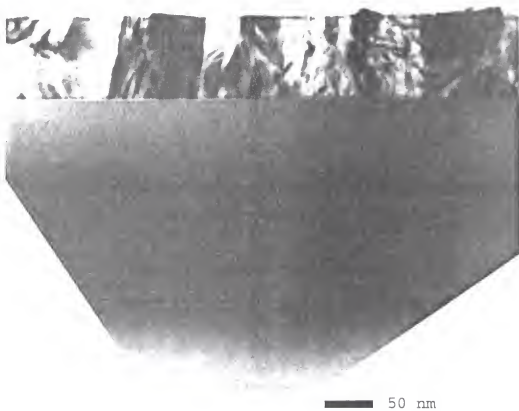


Figure 2-21 Bright field cross-sectional TEM micrograph of laser-annealed sample with intermediate 220 nm-thick oxide layer.

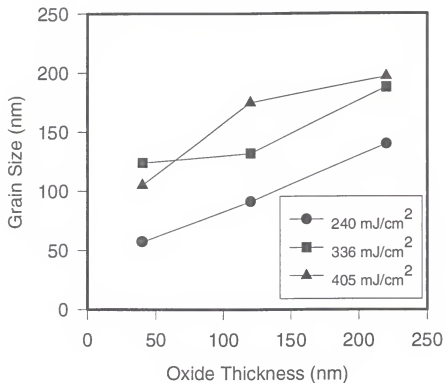


Figure 2-22 Grain size as a function of oxide thickness for samples annealed with various laser energy densities.

CHAPTER 3
EXPERIMENTAL APPROACH

Introduction

In this study, amorphous silicon films deposited on high-quality fused quartz wafers were crystallized using an excimer laser. Research in this area has typically involved direct surface irradiation of the amorphous film with the laser. In this work two unique configurations were used to examine solidification dynamics of the molten films. The conditions for crystallization were (i) through-the-substrate irradiation using special seed wafers in contact with the film surface, and (ii) selective-area crystallization using surface masking of the film during standard laser irradiation. The resultant microstructure of the films was then characterized by transmission electron microscopy (TEM) and scanning electron microscopy (SEM).

Samples

Film samples used in both experiment sets were prepared by low pressure chemical vapor deposition (LPCVD) of silicon onto 675- μm -thick optically-polished high-quality fused silica wafers. Silicon was deposited in an LPCVD system using thermal decomposition of silane [Jae90]:



The deposition was carried out at 600°C, at a deposition rate of 20 nm/min for 20 minutes, resulting in a 400-nm-thick amorphous film.

To facilitate eventual TEM sample preparation, film samples in both experiment sets were cut into one of two shapes. Samples that would eventually undergo plan-view TEM analysis were cut into 3 mm-diameter circular pieces using an ultrasonic cutter. Samples undergoing cross-sectional analysis were cut into 3 x 1 mm rectangular pieces using a diamond wafering saw.

Before laser processing, all samples and seed wafers were cleaned using sonication in acetone then methanol, and then rinsed in deionized water (DI). Samples in the first experiment set also underwent a native oxide removal step consisting of a 30 second dip in 5% HF / 95% DI, followed by

a DI rinse. A discussion of this step is given in the Native Oxide Removal subsection later in this chapter.

In the first experiment set, laser irradiation took place from the substrate side, making substrate energy absorption of the 248 nm radiation a concern. To determine energy loss through the substrate, energy transmission measurements were done before the film deposition. The average energy loss through the SiO_2 substrate wafer was ~10%.

Laser Setup

Laser annealing was performed with a Lambda Physik LPX 305 excimer laser operating with KrF (248 nm) and pulse width ~ 25 ns (FWHM). The beam was collimated using a long focal-length (200 cm) lens. The beam was then focused using a spherical lens with a 25 cm focal length. Distance from the lens to the sample holder was varied to control the energy density at the sample surface. Discharge voltage was also varied in the laser control system to alter the beam energy and hence energy density at the sample. Total energy was measured immediately after the focusing lens to incorporate energy loss through the lenses. All energy measurements were done with a Gentec Sun Series EM-1 laser energy meter equipped with a Gentec ED-500 head. Schematic diagrams of the laser setup are given for each experiment set below.

Seeded Nucleation Experiments

As mentioned in the previous chapter, homogenous nucleation has been observed in pulsed laser annealing of silicon thin films on SiO_2 substrates. The film-substrate interface does not readily offer a location for nucleation. Therefore, the object of this experiment was to examine the effect of intimately joining a small ($\sim 1 \mu\text{m}$) "seed" single-crystal Si surface with the surface of an amorphous Si thin film during irradiation with a pulsed laser. The laser beam was directed through the substrate to allow the seed-wafer at the film surface to affect the nucleation dynamics of the molten film. A schematic of the setup is shown in Figure 3-1. The resultant microstructure of the samples was then characterized using plan and cross-sectional TEM.

Seed Wafers

Seed wafers used in this experiment were fabricated in a class-100 clean room facility in the department of Electrical Engineering at the University of Florida using the following steps, which are outlined schematically in Figure 3-2.

Three-inch diameter, $375\text{-}\mu\text{m}$ -thick single-crystal (100) silicon wafers were used as a starting point (step 1). Approximately 1500\AA of SiO_2 was deposited on them using LPCVD

(step 2). For details on this process see, for example [Jae90 - p. 118]. One micron of AZ 1370 photoresist was then applied using the spin-on technique (step 3). A pre-bake step (90°C/30 min) followed, which prepared the photoresist for the mask-exposure step.

The mask-exposure step was carried out using an industrial stepper which put 100 patterns (individual pattern size on wafer was 1.5 x 1.5 mm) on each wafer. After the masking step, the wafers were developed and post-baked (120°C / 30 min) (step 4). A reactive-ion etch [Gha83] step was used to remove the oxide that was not covered by photoresist (step 5).

A boiling KOH bath was then used to selectively etch in the (100) direction (step 6). The bath consisted of, in volume, 12.5% KOH, 18.5% $(CH_3)_2CHOH$ (isopropyl alcohol), and 69% H_2O . In this bath, the (111) direction etches more than 10 times slower than the (100) because of the higher atomic density [Gha83]. A hydrofluoric-acid dip at this point removed the remaining oxide and photoresist (step 7). The amount of contact area at the top of each of the cone structures was controlled by varying the etching time (4-7 min) in the KOH bath.

Native Oxide Removal

One concern regarding the experimental procedure involves the intimate physical contact that must be established between the seed wafer and the thin film wafer. Freshly cleaved silicon becomes quickly covered with a few monolayers (~ 15-20 Å) of native oxide upon exposure to air and gradually thickens with time to an upper limit of about 40 Å [Gha83]. In order to attain intimate contact between the silicon atoms in seed wafer and the thin film, the oxide layer must be removed. This can be accomplished using an oxide-removal technique [Cha89], which leaves the silicon surface hydrogen-terminated. However, there are some concerns with this technique because though the aqueous HF treatment is known to rapidly etch SiO_2 and not attack Si vigorously [Suz94], it has been shown [Hig90] that the solution can induce microscopic roughness on both Si(111) as well as Si (100).

Weinbereger et al. [Wei86] have supported the idea of fluorine-terminated silicon after HF treatment because of two reasons, (i) the SiF bond strength (~6 eV) as compared to the SiH bond (~3.5 eV), and (ii) given the accepted mechanism of oxide etching, F termination of the silicon interface is expected to be the final step of oxide removal. However, atomic H has been observed on the surfaces consistently [Hig90] and one simple explanation [Uba84] for the observed H termination was given on the basis of infrared measurements of

HF-treated microcrystalline silicon samples. Ubara et al. propose that F-terminated silicon bonds are unstable in an HF solution because of the strong polarization of the Si-Si back bonds facilitating their attack by HF molecules. The resulting reaction,



releases silicon fluoride into solution, leaving a hydrogen-terminated surface behind. The resulting SiH bonds are not attacked because while the reaction $=Si-H + HF \rightarrow =SiF + H_2$ is exothermic, it has an activation barrier which is much higher than that for the Si-Si bond cleavage mentioned previously.

In this work, one major concern regarding the oxide etching and hydrogen termination of the seed wafer and thin film is related to the two silicon surfaces involved. The contact surface of the seed wafer has a (100) orientation, while the thin film is in an amorphous state.

First, a discussion of the (100) surface. As mentioned previously, a silicon surface may be hydrogen-terminated by etching in an HF solution. The resultant surface structure, however, is dependent on the crystal orientation of the silicon. Experimental results [Tak88] from HF-treated (100) surfaces have given a surface structure model, shown in Figure 3-3, which indicate that most of the dangling bonds are

terminated by hydrogen. However, a small fraction are also terminated by fluorine or a hydroxyl group. Also, Si-H bonds are observed which correspond to a (111) plane, suggesting partial existence of non-flat defect areas.

The amorphous surface is expected to have a much less predictable structure. Studies have shown [Cha89] that Si undergoing HF treatment may have surfaces which are microscopically rough, depending on the orientation, and terminate with mono, coupled mono-, di- and trihydride bonds. The amorphous surface will have a varying bond structure and therefore it is expected that once it is HF-treated it will terminate in one of the possible hydrogen bond arrangements, or with a fluorine or hydroxyl group. This should not greatly affect the viability of the seeding effect, however, as there is sufficient thermal energy in the molten film to allow at least some homoepitaxial seeding to occur. At worst, not all of the contact area is necessary for some nucleation effect to take place.

Laser Processing

Laser processing of the seeded nucleation samples was done in the configuration shown in Figure 3-1. All samples were irradiated in air with a single pulse for each sample. As mentioned previously, the laser beam was brought in from the substrate side so the seed wafer in contact with the film

surface may affect nucleation. Given this arrangement, it is worthy to note that complete melting of the film is necessary for the seed wafer to potentially affect nucleation in the molten film. Laser energy densities used for this set of samples ranged from 220 to 420 mJ/cm². Though higher energy densities were initially examined, it was found that values exceeding 500 mJ/cm² caused ablative loss of the film.

Selective Area Crystallization Experiments

Though nucleation is not observed at the interface in the 1-Si/SiO₂ system, it is observed at the 1-Si/a-Si interface [Tsa87]. This is the theoretical driving force for this experiment set. Using 1000-mesh masks, it was possible to selectively melt and crystallize discreet areas on the amorphous film. Since the film areas that were masked did not undergo laser heating and melting, it was expected these a-Si areas would provide nucleation points for the adjacent molten pools thereby creating a novel microstructure. The resultant microstructure of the films samples was examined using plan-view TEM and SEM.

Mask Configurations and Laser Parameters

Masks used in this study are shown in Figures 3-4 and 3-5. The masks are Gilder 1000-mesh copper grids, 3.05 mm O.D., fine bar, 19 μm hole, 6 μm bar width, model #G1000HS, available through Ted Pella, Inc. The two figures shown represent the two sides of the mask, with one side flat and the other having some topography and curvature. Experiments which involved masks in contact with samples had the flat side on the sample.

Three different mask configurations were used in these selective area crystallization experiments. In the first set (contact), the 1000-mesh copper masks were put in direct contact with the sample surface during laser irradiation. A schematic of this arrangement is shown in Figure 3-6. A low energy-absorption (~ 5%) SiO_2 slide was used to hold the mask in direct contact with the sample. Laser energy density values used to crystallize these samples ranged from 230 to 475 mJ/cm^2 .

In the second set (non-contact) the masks were held just off the sample surface. A optical holding mechanism with X-Y adjustment was used to support the mask plane-parallel 1 mm away from the sample surface. A schematic of this arrangement is shown in Figure 3-7. Since this mechanical support mechanism was employed it was not necessary to use the SiO_2 slide used in the contact experiments. Energy density values

used to crystallize the samples in this set ranged from 315 to 440 mJ/cm².

In the third set (variable aperture area), two masks were put together symmetrically, rotated 10° and then glued in place. The resultant structure is shown in Figure 3-8 and it can be seen that the mask openings range in size from almost full-square (19 μm) down to openings of less than 1 μm dimensions. Using this mask arrangement with standard laser irradiation allowed examination of variable crystallized-area effects on resultant microstructure. The SiO₂ slide was used to hold the double mask in direct contact with the sample. Energy density values used ranged from 310 to 480 mJ/cm².

Transmission Electron Microscopy

Transmission Electron Microscopy (TEM) was the dominant characterization technique employed in this work. A JEOL 200 CX tungsten filament 200kV TEM with a point-to-point resolution of 2.3Å was used to acquire all the micrographs shown. The TEM is an extremely diverse instrument capable of many unique characterization techniques and a full discussion of its prowess is best left to the extensive manufacturer literature [Jeo89].

Specimen preparation of the samples for TEM analysis depended on the desired geometry of sample observation. Two

are common: plan view and cross-sectional view. Plan view geometry is useful for analysis of surface films, as the electron beam of the instrument is passing in a direction perpendicular to the film surface, allowing phase contrast at the viewing and camera chamber. In cross-sectional geometry the film/substrate interface is parallel to the direction of the electron beam so that the sample is viewed edge-on. This form is useful for analyzing melt depths as well as grain structure into the film.

Plan view sample preparation began with mechanical polishing of the back of the sample until it was ~ 70 μm thick. The sample was then glued to a PELCO 1GC12H copper grid using Measurements Group Inc. M-Bond 600 adhesive. Samples were then cured for 10 minutes at 90°C. The next part of the thinning process was done with a Measurements Group Inc. dimpler. Samples were dimpled to ~15 μm in the center. The final thinning process was done using a Gatan ion mill via the sputtering action of an Ar^+ ion gun, aimed at the substrate surface, until the specimens were electron transparent.

Cross-section sample preparation consisted of dicing the samples into 3 mm-thick strips using a diamond-blade dicing saw. The strips were then glued together, with M-Bond, and cured for 10 minutes at 90°C. After gluing the samples to the same copper grid as above, they were mechanically polished

until they were ~70 μm thick. They were dimpled the same as plan view samples and final thinning process was done using the Gatan ion mill with two Ar+ ion guns.

Scanning Electron Microscopy

Scanning Electron Microscopy (SEM) [Bru92] was used to examine the surface structure of the laser-annealed films, seed wafers, and copper masks that were used in the masking experiments. A JEOL JSM 6400 operating at 15 kV and a working distance of 15 mm was used to record the micrographs. Some samples were angled 30-45° to accentuate the surface features.

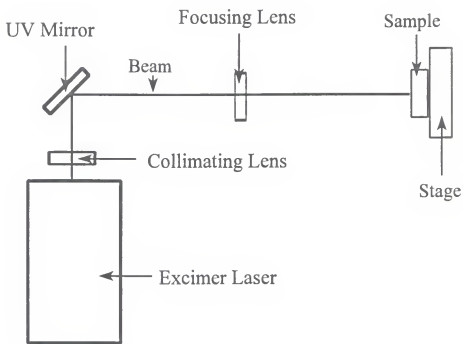


Figure 3-1 Schematic of setup for laser anneal of samples in seeded nucleation experiments.

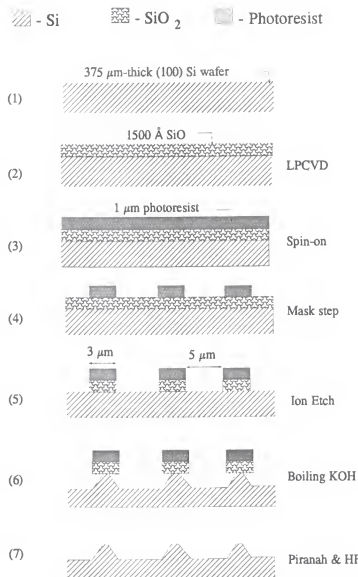


Figure 3-2 Schematic of steps for fabrication seed wafers.

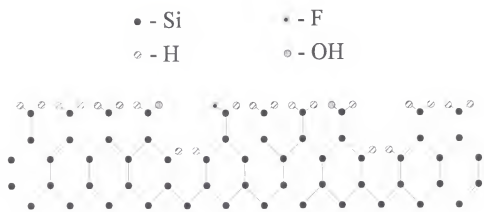


Figure 3-3 Surface structure model of HF-treated (100) silicon showing bonding configuration.

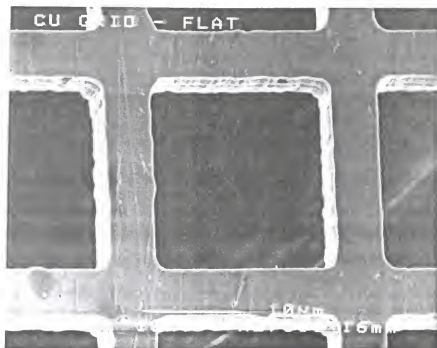


Figure 3-4 SEM micrograph of flat side of copper mask used in selective area crystallization experiments.

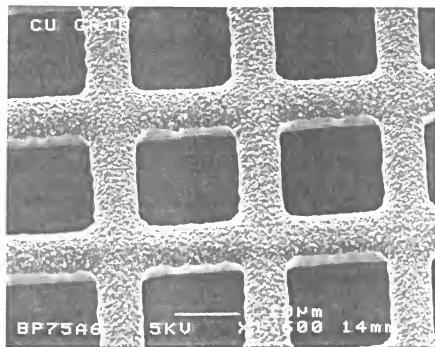


Figure 3-5 SEM micrograph of non-flat side of copper mask used in selective area crystallization experiments.

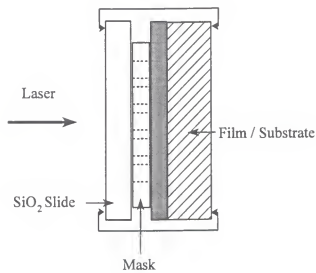


Figure 3-6 Schematic of laser setup for processing of contact selective area samples.

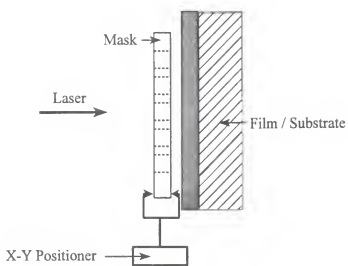


Figure 3-7 Schematic of laser setup for processing of non-contact selective area samples.

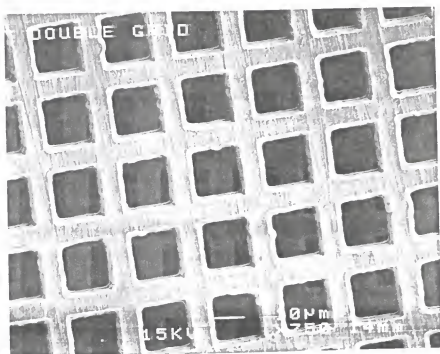


Figure 3-8 SEM micrograph of variable aperture area mask configuration.

CHAPTER 4 RESULTS

Seeded Nucleation Experiments

Seed Wafers

Fabrication of the seed wafers, as outlined in Chapter 3, resulted in the structures shown in Figure 4-1. The pyramid-shaped structure derives its shape from the slow etching of the (111) planes, which are the closest-packed low-index planes [Gha83]. The schematic shown in Figure 4-2 shows the relationship between (100) and (111) planes in a structure etched in this manner. After the seed wafers were fabricated, they were diced into individual units with dimensions 1.5 x 1.5 mm using a diamond-blade wafering saw.

Crystallized Samples

Samples in this experiment set were processed with laser energy densities ranging from 220-420 mJ/cm². Samples were then analyzed using plan-view and cross-sectional TEM. One defining aspect of this set of experiments is related to the maximum melt depth of the film as it is annealed. As

mentioned in Chapter 3, since the laser beam was brought in from the substrate side and the seed wafers were on the surface of the film, complete melting of the film is necessary for the seed to have any effect on the resultant microstructure. In Figures 4-3 and 4-4, representing 220 and 262 mJ/cm², respectively, it is shown that complete melting of the film did not take place. At these two energy densities the melt depths were ~110 and ~175 nm, respectively. Since there was incomplete melting of the film, no seed effect was observed. However, at energy densities sufficient to completely melt the film there was significant effect.

Figure 4-5 shows bright-field plan-view TEM micrographs of a film annealed with an energy density of 338 mJ/cm². The part of the film in direct contact with the seed has delaminated, leaving behind a unique microstructure in the surrounding area. The micrographs shown are typical of what was observed for energy densities above the complete melt threshold. The microstructure is marked by four distinct regions, labeled in the figure.

Region I is defined as the areas at least several microns away from the film/seed contact, and consist of the typically observed laser-annealed microstructure: semi-spherical grains with dimensions on the order hundreds of nanometers. The area immediately adjacent to the delaminated part of the film, Region II, consists of grains with surface dimensions ~0.5 μ m.

Region III, which surrounds the grains in Region II consists of larger grains (~1 μm) and an aspect ratio with the long axis perpendicular to the contact area. The last area of interest, Region IV, occurs inconsistently, and is marked by large (~1.5 μm) rectangular-shaped grains. These grains have the long axis parallel to the contact area.

Selective Crystallized Area Experiments

Before describing the results of this experiment set, it is useful to define some terms used in the morphological descriptions. As mentioned earlier, pulsed excimer laser crystallization of amorphous silicon films (~ 200 nm-thick) using an of energy density ~ 350 mJ/cm² results in a polycrystalline microstructure with grain size on the order of hundreds of nanometers. Under unique conditions some grains will be larger (~ 1 μm) [Im93]. Otherwise, unusual grain sizes are not observed. In the results given in this experiment set there are a number of unique microstructures that to date have not been observed. Terms useful in describing these morphologies include:

1. Standard microstructure - morphology containing semi-spherical grains with dimensions ~ 100-200 nm resulting from the above-mentioned conditions.

2. Enlarged growth - grains with dimensions significantly (factor of 3) larger than standard laser-annealed grains.
3. Anomalous growth - grain or grains having shapes with unusual aspect ratios or geometries which have not been documented previously (see Chapter 2).

Contact Samples

Samples with the mask in contact with the film were processed with laser energy densities ranging from 230 - 475 mJ/cm². The results are given in order of increasing laser energy density. TEM analysis revealed the following microstructures for samples.

In samples irradiated with a laser energy of ~ 232 mJ/cm², ~ 95% of the irradiated regions had the standard microstructure and appear as shown in Figure 4-6. Approximately 5% of the regions observed contained some type of enlarged growth, always at the edge of the irradiated region. An example of this is shown in Figure 4-7. Grains at the corner were relatively large (~ 1 μ m x 0.4 μ m) and appear to have nucleated at the edge. Grains closer to the center of the region were smaller (~ 0.8 μ m x 0.3 μ m) and appear to have nucleated from the inside of the region and solidified outward. The edge grains were smaller as the distance to the corner increased. The rest of the region contained the

standard microstructure.

Using this first sample as a standard, the definition of enlarged edge growth is now given. The enlarged edge growth microstructure consisted of large grains that nucleated at the edge and solidified into the irradiated region. Adjacent to the these grains, were slightly smaller grains that nucleated in the irradiated region and solidified towards the edge, meeting the large edge grains at an interface parallel to the edge.

In samples irradiated with a laser energy of ~ 267 mJ/cm², $\sim 90\%$ of the irradiated regions had the standard microstructure. Approximately 10% of the regions observed contained enlarged grain growth at the edges, similar to that seen in the previous sample. The microstructure shown in Figure 4-8 represents a unique morphology in that area (1) shows multiple nucleation points that are separated from the edge. This differs from the typical enlarged growth microstructure in that area (1) contains a spherical anomalous grain region that is between the grains typically observed. Also, the enlarged growth is observed going into the irradiated region as opposed to remaining on the edge.

In samples irradiated with a laser energy of ~ 310 mJ/cm², $\sim 30\%$ of the irradiated regions showed enlarged edge growth. Most of the growth occurred in the corner regions. Another phenomena which was observed less frequently ($\sim 7\%$ of

regions) is shown in Figure 4-9. This represents an unusual microstructure in that a large-grained region surrounds a very fine-grained central area near the corner. Grains surrounding the fine-grain region are $\sim 0.7 \mu\text{m} \times 0.4 \mu\text{m}$. They appear to have nucleated either at the edge or in the fine-grained region and then solidified towards each other. The fine-grained region in the center is similar to the as-deposited film, which can be seen outside of the irradiated region in any of the micrographs.

In samples irradiated with a laser energy of $\sim 353 \text{ mJ/cm}^2$, $\sim 90\%$ of the irradiated regions showed enlarged edge growth, with $\sim 45\%$ showing internal enlarged growth. One example of this phenomena is shown in Figure 4-10. The edge grains near the corner appear to have the standard enlarged edge growth. However, just inside these grain appears an anomalous spherical region with a two distinct points, labeled area (2). These two points appear to be the nucleation sites for the triangle-shaped grains that solidified outward from them. Above area (2), large grains appeared which have a similar geometry as the enlarged edge growth grains but are away from the edge, in the middle of the irradiated region.

In samples irradiated with a laser energy of $\sim 410 \text{ mJ/cm}^2$, $\sim 95\%$ of the irradiated regions had complete enlarged edge growth, with no anomalous regions observed. An example of the microstructure is shown in Figure 4-11. As already

mentioned, the grains closest to the edge appear to have nucleated in the amorphous region that was masked from the laser. In this sample, however, the grains were ~ 40% larger than those in lower energy density samples. The grains had a length of ~ 1.4 μm in the direction perpendicular to the edge with a width at center of ~ 0.5 μm . The grains predominantly had a triangular shape, with the tip of the triangle at the edge, where the nucleation took place. Once nucleation occurred, solidification took place perpendicular to the edge. The smaller grains adjacent to the edge grains also had a triangular shape, with the tip furthest away from the edge. This is where these grains nucleated and solidified in the direction towards the edge. The long dimension these grains was ~ 0.6 μm .

Non-Contact Samples

Samples with the mask not in contact with the film were processed with laser energy densities ranging from 315 - 440 mJ/cm^2 . TEM analysis revealed the following microstructures for the samples.

Most of the area in samples irradiated with a laser energy of ~ 317 mJ/cm^2 had the standard microstructure. 50-60% of regions, however, had at least one corner which possessed an anomalous enlarged-grain corner structure. The structures were only observed in the corners and one example

of this is shown in Figure 4-12. The top left part of the micrographs is the corner of the irradiated region and some of the as-deposited silicon may be seen there. Adjacent to this area were a few grains typical of the standard microstructure. Adjacent to these were larger grains, area (3), that appear to have nucleated in the transition area. The grains appear to have solidified towards the center of the anomalous structure. Some of these grains were very large (~1.8 x 1.1 μm).

These anomalous corner structures were different from the enlarged edge growth phenomena observed in the contact samples. Since the mask was not in direct contact with the film, the edge effects were not as definitive. However, the interface between masked and non-masked regions did have an effect as the large structures observed in the non-contact samples were always located near a corner.

Samples irradiated with a laser energy of ~ 356 mJ/cm^2 were similar to those just mentioned in that most of the irradiated regions had the standard microstructure and ~ 50-60% of samples had at least one corner which demonstrated anomalous behavior. An example of one of these corners is shown in Figure 4-13. This corner is marked by large (~ 2.2 x 0.7 μm) grains surrounding a region with smaller (~ 1 μm) grains that are triangle-shaped. The center of this region contains a fine microstructure with grain size smaller than the standard microstructure. The large outside grains appear

to have nucleated at the boundary of the structure and solidified inwards. The inner triangular grains appear to have nucleated at the center fine-grained region and solidified towards the outer large grains.

In samples irradiated with a laser energy of ~ 404 mJ/cm^2 , $\sim 75\%$ of the irradiated regions had at least one corner appearing like that shown in Figure 4-14. As in the previous sample, this circular region had large ($\sim 2.5 \times 1.0$ μm) grains in a large circle surrounding an inner region. The inner region contained smaller ($\sim 1 \mu\text{m}$) triangular-shaped grains that appear to have nucleated in the very center region. The center contains a fine-grained microstructure similar to that observed in standard laser annealing. A infrequent variation on this microstructure is shown in Figure 4-15. This structure is similar to the previous two, but the center region is different. In this case the center contains a number of distinct nucleation points where small grains nucleated and solidified.

Samples irradiated with a laser energy of ~ 442 mJ/cm^2 had the most consistent microstructure observed of all the non-contact samples. 95% of the irradiated regions examined looked like that in Figure 4-16. A closeup of one of these corners is shown in Figure 4-17. Though the edges of the irradiated regions in these samples are not as linear as the contact samples, the microstructure is like that of the

enlarged edge growth effect. Large grains ($\sim 2.1 \times 1 \mu\text{m}$) that nucleated at the edge solidified towards the center of the region. These are adjacent to smaller ($\sim 1 \times 1 \mu\text{m}$) grains that nucleated in the irradiated region and solidified towards the large grains. As in the contact samples, there is a distinct interface between these two grain sets.

Variable Aperture Area Samples

Due to the mask arrangement, the crystallized area in these samples varied in size from $\sim 19 \times 19 \mu\text{m}$ for the largest areas down to $\sim 1 \mu\text{m}^2$ regions. This was accomplished by putting two masks together and rotating them slightly off axis, as mentioned in Chapter 3 and shown in Figure 3-8. The microstructure observed in this set of samples varied as a function of energy density and size of crystallized area. Samples with the double mask were processed with laser energy densities ranging from $310 - 480 \text{ mJ/cm}^2$.

Approximately 80% of the irradiated regions observed in samples irradiated with a laser energy of $\sim 308 \text{ mJ/cm}^2$ had the standard microstructure, as shown in Figure 4-18. The rest (20%) of the regions displayed some level of enlarged growth, as shown in Figure 4-19, but there did not appear to be a relationship between the size of the irradiated region and the propensity for enlarged grain growth. Some regions had a combination of microstructure. An example of this is shown in

Figure 4-20. In this case one part of the irradiated region contains the enlarged edge growth observed earlier and the other part has the standard microstructure. As observed previously, the edge grains have the largest long-axis dimensions (~ 0.7 μm) and appear to have nucleated at the edge. Grains farther into the irradiated region have a slightly smaller long-axis dimensions (~ 0.5 μm) and appear to have nucleated furthest away from the edge and solidified towards the it. The two corners appear to be the limits of the propagation for the enlarged growth.

The microstructure of the crystallized regions in samples irradiated with a laser energy of ~ 363 mJ/cm^2 consisted of a combination of standard microstructure and enlarged edge growth areas. Most (~ 80%) irradiated regions demonstrated a combination of microstructures and there was no relationship between size of area annealed and propensity for enlarged growth. However, in regions that were smaller (~ 5 x 5 μm) the enlarged edge growth effect occupied a greater percentage of total annealed area. An example is shown in Figure 4-21. This micrograph shows an area that is ~ 4 μm along the short axis and has the enlarged edge-effect grains (~ 1 x 0.5 μm). As seen previously, next to these large grains are the slightly smaller (~ 0.8 x 0.4 μm) grains that have nucleated farther away from the edge but appear to grow in the direction of the edge. The other edge of the region has the standard

microstructure. An example of a smaller crystallized region is shown in Figure 4-22. This micrograph represents one of the smallest irradiated areas in the experiment. The entire region is $\sim 1.6 \mu\text{m}$ in diameter. The grains appear to nucleate predominantly at the edge and solidify towards the center. The larger grains have dimensions $\sim 0.7 \times 0.2 \mu\text{m}$.

Most ($\sim 90\%$) of the crystallized areas in samples irradiated with a laser energy of $\sim 409 \text{ mJ/cm}^2$ had the standard microstructure with some form of enlarged edge growth. As in the previous samples, crystallized regions with smaller dimensions did not necessarily have a greater propensity towards enlarged growth but the enlarged growth that did occur constituted a large percentage of the region. Figure 4-23 is an example of this. In this micrograph large ($\sim 1 \times 0.5 \mu\text{m}$) grains are observed in one side of the area while the other size had the standard microstructure. In this particular area, however, the size of the annealed region affected the solidification dynamics. The grains along the perimeter have the geometry observed in the enlarged edge growth but the grains inside of these are different. They are larger ($\sim 1.4 \times 0.8 \mu\text{m}$) than the edge grains and have various orientations.

The final samples in this set of experiments were irradiated with a laser energy of $\sim 479 \text{ mJ/cm}^2$ and had the most consistent microstructure. Enlarged edge-effect grains

were observed in all crystallized areas. In regions where the crystallized area was smaller there was only enlarged edge growth grains and no standard microstructure observed. Shown in Figure 4-24 is a crystallized region with dimensions $\sim 6 \times 2 \text{ }\mu\text{m}$. Only the enlarged grains are observed, with grains appearing to have nucleated on the edge of the region and solidified towards the center. Grains on both sides of the center line appear to have equal dimension ($\sim 1 \text{ }\mu\text{m}$) along the long axis.

In crystallized areas with slightly larger dimensions, the transition from all enlarged edge-effect microstructure to a combination of enlarged and standard is observed. An example of this is shown in Figure 4-25. The size of this crystallized region is $\sim 7.8 \times 7.6 \text{ }\mu\text{m}$. Along the edges of the area there are the large ($\sim 1.8 \times 0.6 \text{ }\mu\text{m}$) edge grains typically observed, with smaller ($\sim 0.7 \times 0.5 \text{ }\mu\text{m}$) grains inside of the larger. As usual, nucleation occurs at the edge for the large grains and inside the area for the small grains. In this case in the center of the region there is a $\sim 1.7 \text{ }\mu\text{m}$ square area consisting of the standard microstructure.

Crystallized areas with even larger dimensions consistently demonstrated the enlarged edge-effect grain structure. An example of this is shown in Figure 4-26. This region is $\sim 15 \times 9 \text{ }\mu\text{m}$ in size. Grains nucleated at the edge have a long axis dimension of $\sim 1.6 \text{ }\mu\text{m}$ and the inside, smaller

grains that nucleated closer to the center have a long axis dimension of ~ 0.8 μm . This approximately 2:1 ratio of long axis dimension of the large and small grains was observed consistently through contact laser-crystallized samples.

A small (~ 5%) number of the crystallized regions observed in this sample had an anomalous microstructure. An example of this unique effect is shown in Figure 4-27. The edge grains in the left portion of the micrograph are longer than usual (~ 2.4 μm), and the standard smaller grains are not adjacent to them. Instead, there are to be four internal nucleation points which affected the solidification dynamics of the system. These four points have provided nucleation locations for the triangular grains surrounding them. Farther to the right there is another anomalous structure. On the right edge of the crystallized region the standard edge-effect grains are observed. To the left are the smaller grains typically associated with the enlarged edge growth grains. However, an area with the standard microstructure is adjacent to this and extends into the area next to the four nucleation points mentioned earlier. These four points have affected solidification in the system in such a way as to allow proliferation of the enlarged grain mechanisms to proceed in an atypical fashion. In order for this to occur the nucleation at these points must have occurred on the same time scale as nucleation at the edges.



Figure 4-1 SEM micrograph of seed wafer fabricated lithographically and used in the seeded nucleation experiments.

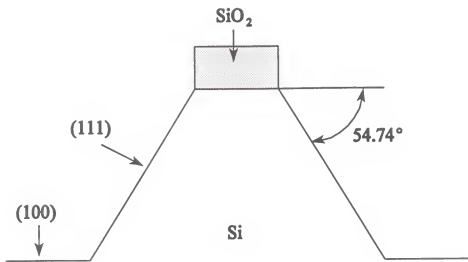


Figure 4-2 Schematic relationship between (100) and (111) planes in silicon during the KOH etch step.

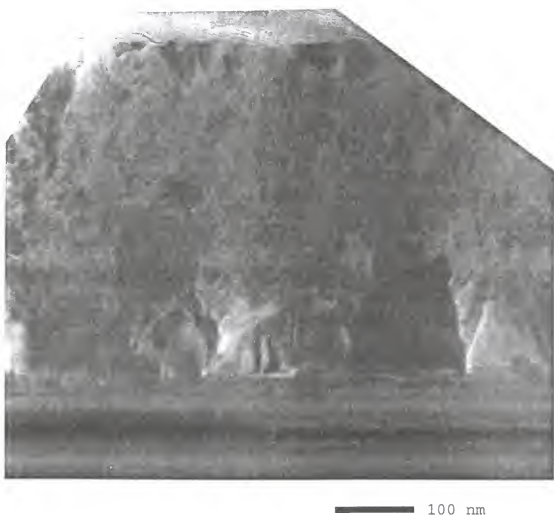
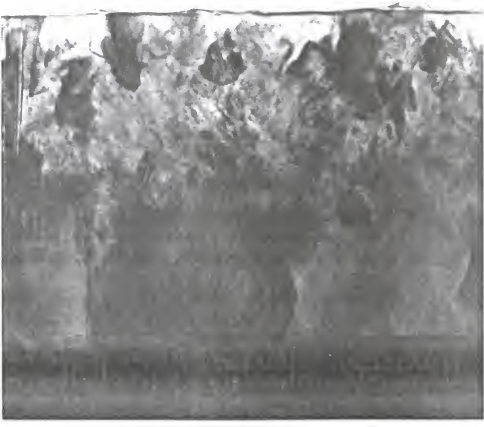


Figure 4-3 Cross-sectional TEM micrograph of silicon film irradiated through the substrate at 220 mJ/cm^2 .



100 nm

Figure 4-4 Cross-sectional TEM micrograph of silicon film irradiated through the substrate at 262 mJ/cm^2 .

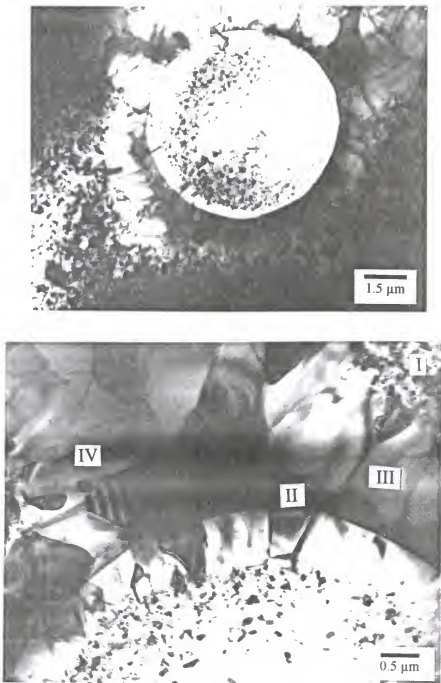


Figure 4-5 Plan-view TEM micrographs of silicon film irradiated through the substrate at 338 mJ/cm^2 using the seeded nucleation process.



Figure 4-6 Plan-view TEM micrograph of selective crystallized area sample irradiated with 232 mJ/cm^2 .



Figure 4-7 Plan-view TEM micrograph of selective crystallized area sample irradiated with 232 mJ/cm^2 .



Figure 4-8 Plan-view TEM micrograph of selective crystallized area sample irradiated with 267 mJ/cm^2 .

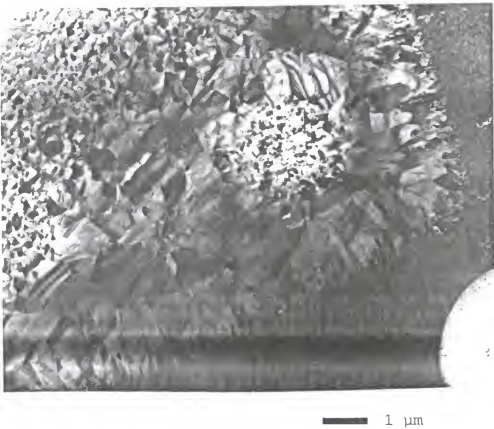


Figure 4-9 Plan-view TEM micrograph of selective crystallized area sample irradiated with 310 mJ/cm^2 .



Figure 4-10 Plan-view TEM micrograph of selective crystallized area sample irradiated with 353 mJ/cm^2 .

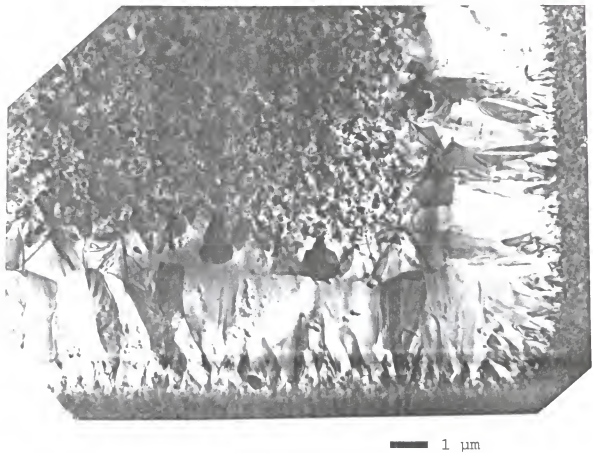


Figure 4-11 Plan-view TEM micrograph of selective crystallized area sample irradiated with 410 mJ/cm^2 .



Figure 4-12 Plan-view TEM micrograph of selective crystallized area sample irradiated with 317 mJ/cm^2 .

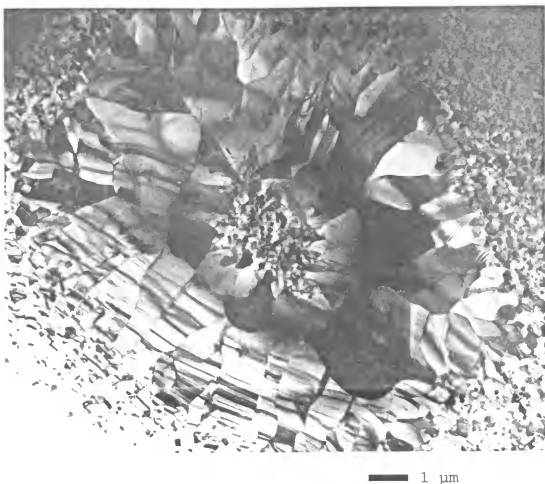


Figure 4-13 Plan-view TEM micrograph of selective crystallized area sample irradiated with 356 mJ/cm^2 .

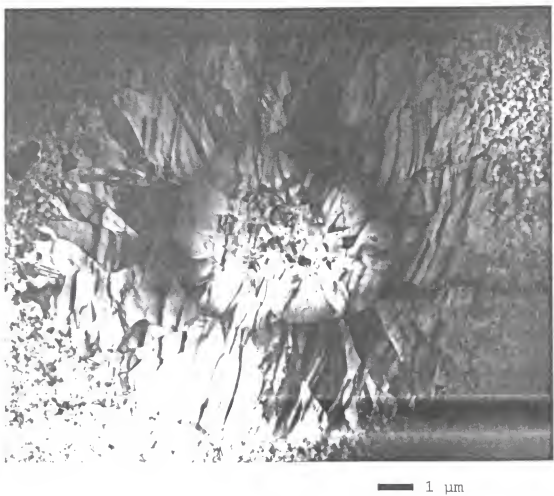


Figure 4-14 Plan-view TEM micrograph of selective crystallized area sample irradiated with 404 mJ/cm^2 .



Figure 4-15 Plan-view TEM micrograph of selective crystallized area sample irradiated with 404 mJ/cm^2 .

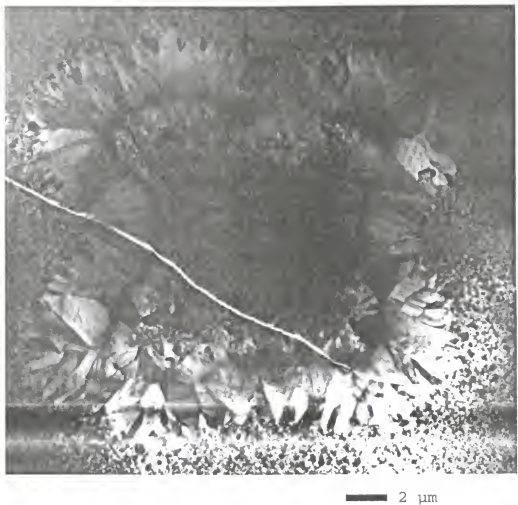
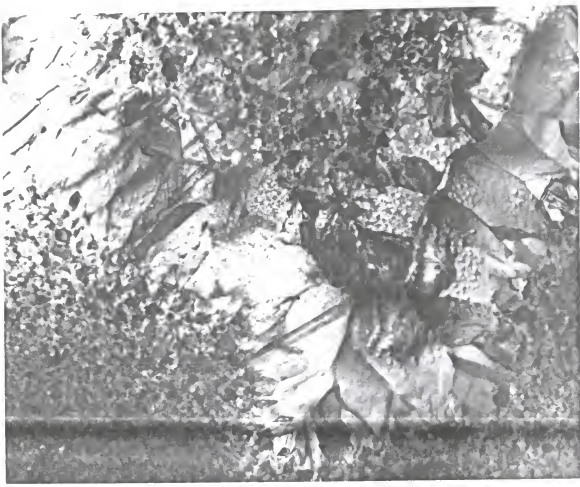


Figure 4-16 Plan-view TEM micrograph of selective crystallized area sample irradiated with 442 mJ/cm^2 .



— 1 μm

Figure 4-17 Plan-view TEM micrograph of selective crystallized area sample irradiated with 442 mJ/cm^2 .

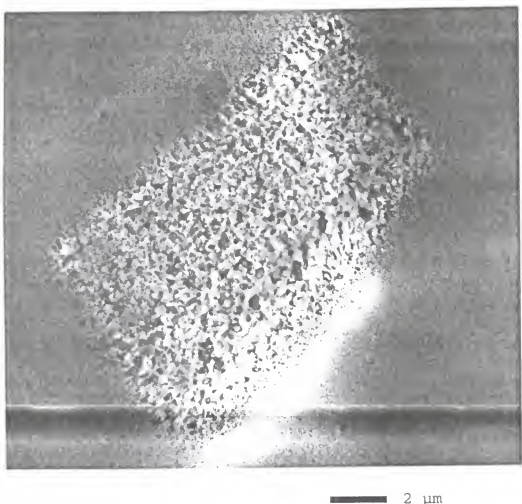


Figure 4-18 Plan-view TEM micrograph of selective crystallized area sample irradiated with 308 mJ/cm^2 .



Figure 4-19 Plan-view TEM micrograph of selective crystallized area sample irradiated with 308 mJ/cm^2 .

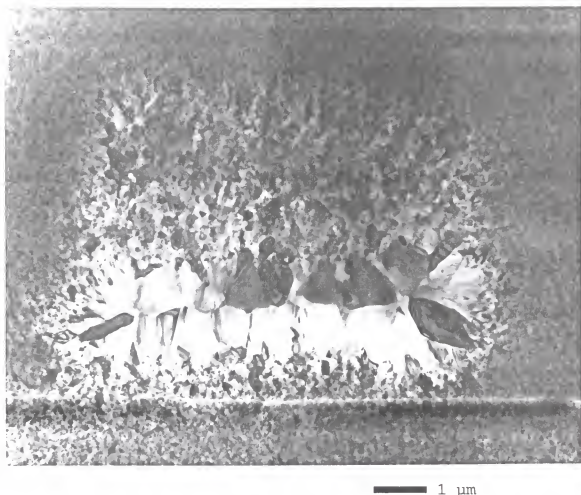


Figure 4-20 Plan-view TEM micrograph of selective crystallized area sample irradiated with 308 mJ/cm^2 .

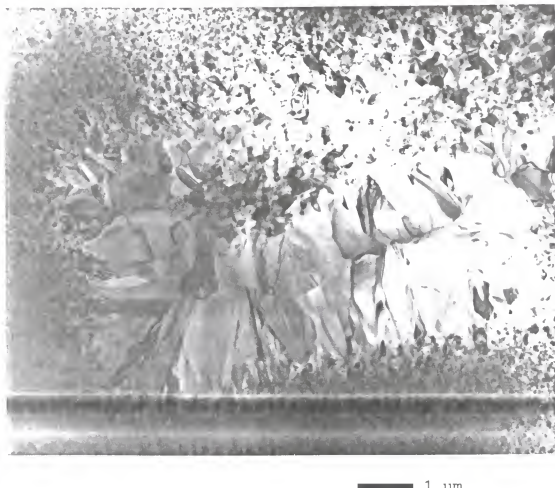
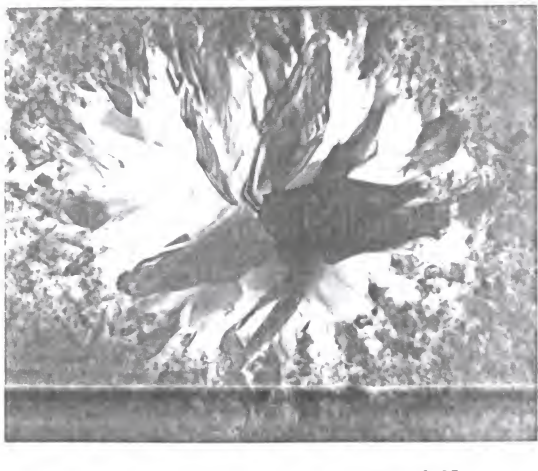


Figure 4-21 Plan-view TEM micrograph of selective crystallized area sample irradiated with 363 mJ/cm^2 .



— 0.25 μ m

Figure 4-22 Plan-view TEM micrograph of selective crystallized area sample irradiated with 363 mJ/cm^2 .



Figure 4-23 Plan-view TEM micrograph of selective crystallized area sample irradiated with 409 mJ/cm^2 .

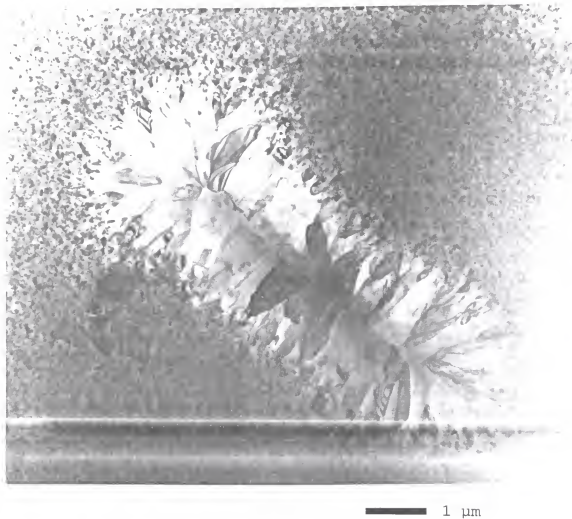


Figure 4-24 Plan-view TEM micrograph of selective crystallized area sample irradiated with 479 mJ/cm^2 .

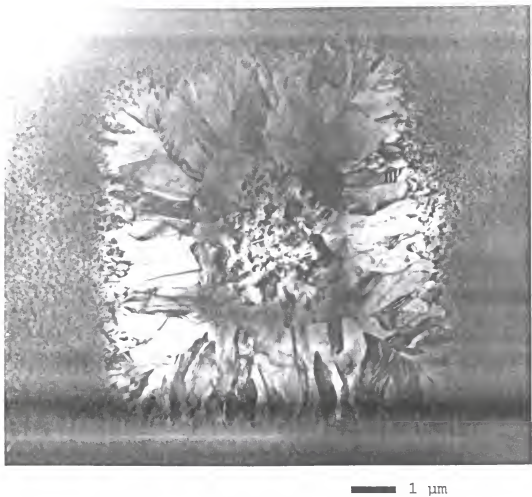


Figure 4-25 Plan-view TEM micrograph of selective crystallized area sample irradiated with 479 mJ/cm^2 .

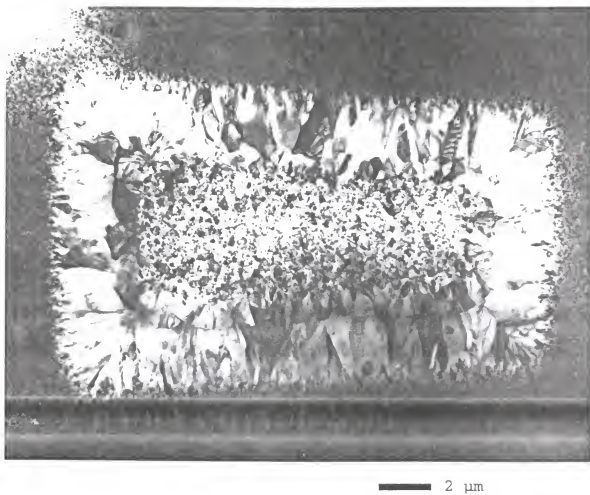


Figure 4-26 Plan-view TEM micrograph of selective crystallized area sample irradiated with 479 mJ/cm^2 .

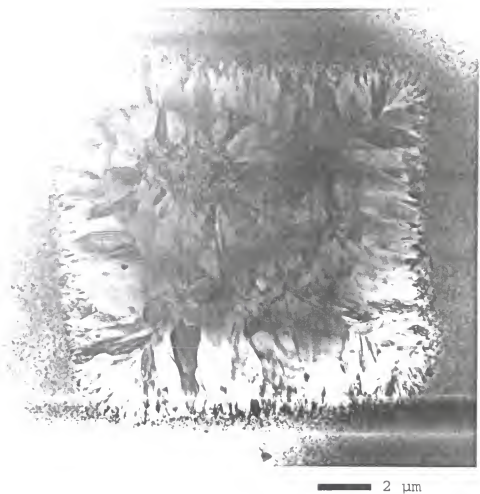


Figure 4-27 Plan-view TEM micrograph of selective crystallized area sample irradiated with 479 mJ/cm^2 .

CHAPTER 5 DISCUSSION

Solidification of Laser-Melted Silicon Films

Understanding of the solidification mechanisms during pulsed-laser processing of silicon films requires a knowledge of the relationship between the interface velocity and the interface temperature. This chapter begins with an analysis of the driving forces for interface motion during solidification, followed by a technical discussion of the evolution of microstructure of the samples in this work.

To begin, interface motion is governed by (i) the thermal gradient established during laser irradiation (thermodynamic effect) and (ii) the molecular kinetics across the interface (kinetic effect).

Thermodynamics

The thermodynamic driving force for solidification is the reduction ΔG in free energy upon changing phase from liquid to solid at temperatures below the equilibrium melting point, T_m . The velocity of the liquid-solid interface is determined by the rate of heat extraction from the interface into the

bulk. This rate depends on the temperature gradient just behind the interface $(\partial T / \partial z)_i$, and a simple relationship correlates velocity, u , with the gradient [Bae82] :

$$u = \frac{\kappa}{\Delta H_m \rho} \left(\frac{\partial T}{\partial z} \right)_i \quad (5.1)$$

where κ is the thermal conductivity in the interface region at T_m , ΔH_m the latent heat of melting, and ρ the density. If the temperature gradient in the liquid phase is assumed to be zero, the only way to change the velocity value is through the interface term, $(\partial T / \partial z)_i$. In the case of melting silicon thin films on nonreactive substrates by pulsed-laser radiation, large thermal gradients in the underlying substrate cause the molten film to cool rapidly ($\sim 10^7$ - 10^9 K/s) [Sti91]. The resulting velocity is then on the order of several meters per second.

Temperature distribution in a laser-melted system is determined by the competition between the rate of energy deposition and the rate of heat diffusion. The liquid-solid interface velocity is therefore a function of the pulse duration and thermal diffusivity of the bulk. With regards to the latter, if the film is fully molten the thermophysical properties of the substrate will affect the quench rate. The quench rate of a molten film is determined by the thermal flux to the substrate and the thermal capacity of the film [Via96],

and therefore substrate choice controls one aspect of the interface velocity.

The other controlling force in temperature distribution is pulse duration. Research in this area [Bae82] show interface velocities of 10, 6, and 3 m/s for pulse lengths of 2.5, 15, and 100 ns, respectively, for equal melt depths. In the case of near melt-threshold energy densities, melt lifetimes occur in a temporally comparable manner to the pulse length and therefore the temperature distribution is determined by the rate of heat deposition. Temperature gradients can be related to melt temperature and characteristic heat diffusion length ($2D\tau$)⁵:

$$\left(\frac{\partial T}{\partial z}\right)_i \sim \frac{T_m}{\sqrt{2D\tau}} \quad (5.2)$$

where D is the heat diffusivity and τ is the pulse duration in seconds. For melt lifetimes which exceed pulse duration, the relation above may be adjusted by replacing the pulse duration term, τ , with melt lifetime values. Time-resolved reflectance and conductance measurements [Aus78, Low88, Tho83] show an increase in melt lifetimes from tens to hundreds of ns with an increase in energy density. These values represent significantly longer times than standard

excimer laser pulse lengths (~ 30 ns).

Kinetics

As mentioned, interface motion is also governed by molecular kinetics across the solid-liquid interface during solidification. The velocity of a planar liquid-solid interface can be expressed in terms of the free energy change as [Gal85]:

$$u = F(T_i, \Delta G, \dots) [1 - \exp(-\Delta G/kT)] \quad (5.3)$$

where T_i is the interface temperature and ΔG is the phase change free energy. This equation shows that as ΔG increases, the solidification velocity will increase up to some value determined by the function F . There are many theoretical views on what terms the function should contain, but typically it contains the distance which the interface moves per solidification event and the probability of the event occurring.

Thompson et al. [Tho85] define the interface solidification velocity from general kinetic arguments. They begin with the assumption of steady state where the interface motion satisfies $u\Delta H = \kappa(\partial T/\partial z)$, as given earlier. If the latent heat release by the interface velocity, $u\Delta H$, does not equal the heat flow required by thermal conduction, the interface temperature will increase or decrease until the

steady state condition is established. The relationship between the velocity of the liquid-solid interface and its temperature is given as:

$$u = f\lambda\omega \exp(-\Delta Q/RT_i) [1 - \exp(-\Delta G/RT_i)] \quad (5.4)$$

where f is a site fraction, ω is an attempt frequency, λ is an average jump distance, ΔQ is an activation energy, and ΔG is the change in Gibbs free energy during the phase change. For small undercoolings, the interface velocity is approximately linear with the undercooling $\Delta T = T_i - T_m$ and the interface velocity near T_m can be defined:

$$u \text{ (m/sec)} = 6.4 f \exp(-\Delta Q/kT_i) \Delta T \quad (5.5)$$

However, in this analysis the $\lambda\omega$ product is approximated as the speed of sound in the liquid, which is a reasonable assumption for low viscosity elemental systems, but gives the unphysical result that the melting velocity can exceed the sound velocity under conditions of extreme overheating [Pee87].

Interface Response Function

Peercy et al. [Pee87] also define u but approach the relationship between the interface velocity and the interface temperature with the use of the interface response function. This function fundamentally describes the kinetics of liquid-

solid transformations during solidification. There have been previous experimental measurements of the interface response function but they were confined to viscous systems in which the interface velocity changes relatively slowly with temperature. In low viscosity elemental systems the rapid change of velocity with temperature has limited experimental study. Technological advancements in the 1980s allowed accurate transient conductance and reflectivity measurements [Sti91, Tsa88, Low88, Gal85, Sti90] from which solidification velocities were numerically derived. Nanosecond-resolution x-ray diffraction has been used to measure interface and lattice temperatures of silicon during pulsed-laser induced melting [Lar88], and more recently, transient thermal emission and emissivity measurements [Xu94] have also allowed direct measurement of the solid-liquid interface temperature during laser melting. These real-time measurements can be used to estimate the interface response function far from equilibrium.

The theoretical approach of the interface response function assumes that the liquid to solid transformation is mediated by a transition state. The intent is to relate the thermodynamic driving force for solidification ΔG to the interface velocity while including kinetic and transition state terms. In classical transition state theory [Spa82], the velocity of a planar liquid-solid interface is given by:

$$U(T) = f\lambda\omega \exp(-\Delta G^*/kT_i) [1 - \exp(\Delta G/kT_i)] \quad (5.6)$$

where ΔG^* is a transition state free energy barrier referenced to the liquid. Assuming small deviations of interface temperature from the melting temperature, the equation is expanded about T_m to yield the solidification velocity as:

$$U(T) = f\lambda\omega \exp(-\Delta G^*/kT_i) [\Delta H_{ls}/kT_m T_i] (T_m - T_i) \quad (5.7)$$

$$\sim \beta (T_m - T_i) \quad (5.8)$$

where β is the slope of the interface-velocity response function near T_m . This approach allows the use of transient measurements to determine β . Two sets of results were derived using this technique, one from transient conductance measurements and the other from X-ray diffraction studies. The conductance measurements give melt depth as a function of time, from which solidification velocity can be derived. Nanosecond-resolution x-ray diffraction analysis [Lar88] provide interface and lattice temperatures during laser annealing which can be used to numerically estimate velocities.

The results derived from transient conductance measurements relate undercooling ΔT and interface velocity v as:

$$v = (0.07 \pm 0.03) (T_m - T_i) \text{ (m/s) / K} \quad (5.9)$$

while the X-ray diffraction data resulted in the relation:

$$v = (0.06 \pm 0.02) (T_m - T_i) \text{ (m/s) / K} \quad (5.10)$$

Both cases contain several approximations and therefore they are in agreement within experimental uncertainty. However, while these results yield insight into the mechanisms, assumptions are made that do not apply to all laser-induced melting scenarios. For example, it was assumed that no laser energy was deposited during the time the interface velocity increased from zero to its maximum value, ie. very short laser pulse (< 10 ns). This is not directly applicable for excimer lasers which have pulse lengths 25 - 45 ns (FWHM).

Seeded Nucleation Experiments

In the previous section, current theories regarding solidification velocity were discussed. In this section and the next, the evolution of microstructure in the experiments outlined in this work is discussed. One interesting point that

must be made is that analysis of the microstructure of these samples incorporates an examination of multiple phenomena. In both experiment sets, distinctive solidification scenarios prevent the direct use of simple models. However, the evolution of microstructure can be explained in terms of a combination of transient thermodynamic and kinetic mechanisms.

The microstructure and grain growth observed during seeded irradiation can be explained in terms of transient heat-flow phenomena and nucleation kinetics. In Figure 4-5, Region I, containing the standard laser-annealed microstructure, is not affected by the thermal effects of the seed. The sphere of influence for thermal transport for the seed contact is limited to the thickness of the film and 2-4 μm in the lateral direction. This lateral value is confirmed by calculations of characteristic heat diffusion length [Via94] using typical melt lifetime values (~200-300 ns) in place of pulse duration.

Region II, containing grains adjacent to the area in contact with the seed, is of significant interest. Since the neighboring contact area delaminated in an angled fashion, it is possible to see a cross-sectional view of the film. The grains in this region nucleated close to the substrate and, as their shape reveals, solidified radially away from the contact area. As enthalpy was released at the interface of these growing grains, the solidification velocity decreased. Due to

this temperature increase at the interface, nucleation did not occur there, but farther away radially from the contact region. While the grains in this region nucleated and grew, the molten film surrounding it cooled due to the thermal losses to the substrate. The ensuing thermal gradient provided the growth scenario for the grains in Region III.

Region III surrounds Region II and consists of relatively large grains that solidify primarily perpendicular to the contact area. The thermal gradient caused by release of enthalpy in Region II prevented nucleation in the immediate area, but in doing so promoted growth for grains nucleating $\sim 1 \mu\text{m}$ away. Support of this idea includes (i) the liquid that ultimately becomes Region III can be undercooled due to lack of nucleation at the film/substrate interface [Sin88], and (ii) nucleation will not occur on the face of the solidified grain in Region II because the energy of interface disordering is large [Haj94].

The last region of interest, Region IV, occurred inconsistently. It is marked by large rectangular-shaped grains whose long axis is parallel to the seed contact edge. The grains nucleated on the outer fringes of the region and solidified towards the center, where they collided during growth. Their dimensions on the average were larger ($\sim 1.5 \mu\text{m}$) than those of the grains observed in Region III. The evolution of this part of the microstructure was dictated by

the grain shape in Region III. Anomalous Region IV grains were only observed where Region III grains did not nucleate ~ 1 μm away radially from Region II. Instead, the Region III grains had a long-axis grain boundary tangential to the contact area. This boundary prevented localized nucleation, due to enthalpy release, and created a thermal gradient parallel to it that promoted the anomalous Region IV growth. This phenomena appears to have continued and propagated substantially away ($\geq 3 \mu\text{m}$) from the contact area.

Selective Crystallized Area Experiments

In this section, the evolution of microstructure in the selective crystallized area experiments is discussed and modeled. The modeling approach involves analyzing the most consistent microstructure observed and its evolution. Modeling this system is a two-dimensional heat-flow problem due to the edge effects caused by the non-irradiated amorphous Si region. Compounding the difficulty of the analysis is the nucleation phenomena observed. As mentioned in Chapter 2, molten Si films do not readily nucleate on SiO_2 substrate interfaces, but do at a-Si interfaces. The modeling approach has to take this into consideration. Also, undercooling on the order of several hundred degrees has been well documented in laser melting of

Si films on SiO_2 , further complicating the modeling.

Designing the model involves defining an effective thermal conductivity for the system at various locations, and solving the heat-flow equation using a one-dimensional finite-difference computer-based simulation, developed by the author and his advisor. This simulation is able to model the effect of laser interactions with multi-layered structures. Details are given in the Appendix.

The one-dimensional simulation is used to model the thermal history of various locations of the annealed region, incorporating edge effects accordingly. In doing so, a general temperature profile at various times can be calculated and used to develop the sequence of events resulting in the observed microstructure. A discussion of the evolution of the anomalous microstructures observed is presented at the end of the section.

Evolution of Microstructure

To analyze the evolution of microstructure in this experiment set, it is useful to determine the most consistent aspect of the microstructures studied. Though there were a number of samples with anomalous features, the enlarged growth edge effect, described in Chapter 4, was observed in almost all samples annealed at the higher laser energy ($>350 \text{ mJ/cm}^2$) densities. The focus of this analysis is microstructures that

adjacent to a smaller (0.5-1 μm) grains just inside the perimeter of the large grains. The large grains nucleated at the a-Si interface, while the smaller inner grains nucleated inside the irradiated region. This effect was observed in the contact samples (see Figure 4-11), non-contact samples (see Figure 4-16), and variable aperture area samples (see Figure 4-26).

Figure 4-26 most clearly exemplifies this effect and is the reference for the model. A schematic of this microstructure is shown in Figure 5-1. The edge grains average $\sim 1.6 \mu\text{m}$ in the direction normal to the a-Si interface. The smaller grains inside of the edge grains average $\sim 0.8 \mu\text{m}$ in the same direction. The edge grain/inside grain interface is distinctive in this and other micrographs (Figures 4-11 and 4-17) showing the enlarged edge effect. This allows the system to be considered as two solidification fronts, with characteristic growth distances, that meet at a distinct interface. The area inside the grain regions has the standard microstructure, and was apparently not affected by the a-Si region during solidification.

A description of the evolution of the microstructure is as follows. After the film is fully molten and the laser pulse is over, cooling begins. The inner region, which ultimately has the fine-grained microstructure, represents that commonly observed in laser annealing of a-Si films on SiO_2 . The

mechanisms leading to the final microstructure have been actively studied [Cho94, Im93, Nar85, Win90], and were outlined in detail in Chapter 2. Fully-molten films cool with thermal conduction to the substrate and undercool several hundred degrees before homogeneous nucleation takes place. Recalescence occurs and is followed by steady-state solidification. This process takes place in ~ 350-400 ns [Xu94] for 400 nm-thick films irradiated with excimer laser energy densities just sufficient for complete melting. The resultant microstructure consists of equiaxed fine grains with dimensions on the order of 200-300 nm.

Regions that are close to the edge of the irradiated region undergo a vastly different microstructural evolution. Two reasons for this are (i) nucleation occurs readily at the a-Si/1-Si interface, and (ii) enhanced thermal loss to the a-Si region. The thermal flux out of the molten film near the edge of the irradiated region has two components (i) the flux into the SiO_2 substrate, J_{SiO_2} , and (ii) the flux into the amorphous Si region, $J_{\text{a-Si}}$. A schematic of the thermal flux components is shown in Figure 5-2. From this figure the total flux out of the grain region, J_{total} , can be defined as the sum of both components:

$$J_{\text{total}} = J_{\text{SiO}_2} + J_{\text{a-Si}} \quad (5.11)$$

Flux into the SiO_2 substrate, J_{SiO_2} , is defined as [Woo86]:

$$J_{SiO_2} = K_{SiO_2} \left(\frac{\partial T}{\partial x} \right)_{SiO_2} \quad (5.12)$$

where K_{SiO_2} is the thermal conductivity of the substrate and $(\partial T / \partial x)_{SiO_2}$ is the thermal gradient in the substrate.

Defining the thermal flux into the amorphous Si region is not as simple because it is a temporally and spatially transient effect. However, this effect can be incorporated by including a term defining the heat diffusion length of the region next to the a-Si, $(D_g t)^{0.5}$ [Poa82], where D_g is the heat diffusivity of the grain region and t is the time. The term also includes the a-Si film thickness, h . With this approach, the flux into the amorphous region, J_{a-Si} is defined as:

$$J_{a-Si} = \frac{h}{\sqrt{D_g t}} K_{a-Si} \left(\frac{\partial T}{\partial x} \right)_{a-Si} \quad (5.13)$$

Combining (5.12) and (5.13):

$$J_{total} = K_{SiO_2} \left(\frac{\partial T}{\partial x} \right)_{SiO_2} + \frac{h}{\sqrt{D_g t}} K_{a-Si} \left(\frac{\partial T}{\partial x} \right)_{a-Si} \quad (5.14)$$

Using (5.11) and (5.12), an effective thermal conductivity, K_{eff} , can be defined:

$$K_{eff} = \frac{J_{total}}{\left(\frac{\partial T}{\partial x} \right)_{eff}} \quad (5.15)$$

Now that an effective thermal conductivity has been defined, several parameters must be addressed. First, the thermal gradient ($\partial T / \partial x$) values for the SiO_2 substrate and the amorphous Si region must be defined. These values change as a function of time, but can be derived using the laser-interaction simulation. Calculations were performed for SiO_2 and a-Si substrates and thermal gradient values in the substrate as a function of time are shown in Figure 5-3. Thermophysical properties used in the simulation for the materials systems are detailed in the Appendix.

Thermal conductivity values vary as a function of temperature for both a-Si and SiO_2 , and are given by [Fog93]:

$$K_{a-Si}(T) = 2.5 \times 10^{-5} T + 0.018 \quad \left[\frac{W}{cm \cdot K} \right] \quad (5.16)$$

and

$$K_{\text{SiO}_2}(T) = 1.5 \times 10^{-5} T + 0.0084 \quad \left[\frac{W}{cm \cdot K} \right] \quad (5.17)$$

Since analytical equations are used in part to derive effective values, these temperature-dependent terms must be averaged over the range of interest, 300-1420 K. This temperature range has been chosen because it represents (i) the initial temperature, 300 K, and (ii) the temperature at which the center region melts, 1420 K [Sti91]. To determine

the average solid phase value of the thermal conductivity of the a-Si region and the substrate, the following equation is used [Sin96]:

$$K_s = \left(\frac{\int_{T_1}^{T_M} \frac{1}{K}(T) dT}{T_M T_1} \right)^{-1} \quad (5.18)$$

Performing this step for the thermal conductivity of the substrate and the a-Si region yields values of 0.020 and 0.038 (W/cm·K), respectively. With the thermal gradient values defined and effective thermal conductivity values established, the last step is to define the effective thermal gradient value. The approach in this model is to consider the system as a one-dimensional heat flow scenario, with an SiO_2 substrate. Therefore, SiO_2 thermal gradient values derived from the simulation are used. As can be seen from Figure 5-3, there is not a large difference in thermal gradient values between the a-Si and SiO_2 substrates.

Incorporation of the effective thermal conductivity involves an iterative approach. First, temperature profiles during and immediately after the pulse are examined. In Figure 5-4 are shown the temperature profiles ($t = 5$ ns) of a (i) 400 nm-thick a-Si film on an SiO_2 substrate, irradiated with a 700 mJ/cm², 25 ns (FWHM) rectangular pulse, and (ii) 400 nm-thick a-Si film on an a-Si substrate, irradiated with the same

pulse. This time was chosen to show the point at which surface melting begins. This figure also shows the dramatic temperature profile resulting from the high absorption coefficient which all phases of Si demonstrate. The laser energy density value used in the simulation is higher than that in the experiment. The reason for this is that the beam has a Gaussian profile (as shown in Figure 2-1) and the samples were processed in the center of the beam. Energy measurements average over the entire beam area, resulting in the difference.

In Figure 5-5 are shown the temperature profiles, for various times, of a 400 nm-thick a-Si irradiated with a 700 mJ/cm², 25 ns (FWHM) rectangular pulse. This figure shows that complete melting of the film does not occur until after 30 ns. Also, the film is at least half solid until ~ 20 ns. Using $D_a = D_{a-Si}$ and equation (5.15), the first K_{eff} value is 0.065 (W/cm·K). Using this value in the simulation, the temperature at the edge can be calculated and compared with the temperature in the center region.

After the pulse is over, cooling begins and the edge reaches the equilibrium crystallization temperature (1685 K) at 30.5 ns. At this same time, the center region is at ~ 1710 K. A temperature profile across the irradiated region is shown in Figure 5-6(a), including thermal diffusion distances for the solidifying region. Nucleation occurs at the edge and

solidification in the direction perpendicular to the a-Si interface begins after the center region passes the equilibrium melt temperature, as shown in Figure 5-6(b).

Cooling continues in the center region, creating a thermal gradient that drives the solidification of the edge grain. Figure 5-7(a) shows the temperature profile at 35 ns. The thermal gradient driving force at this point is 5.5×10^5 K/s. Using (5.10), a solidification velocity can be estimated at ~ 3.3 m/s. This velocity continues to increase because the center region cools until it reaches some homogeneous crystallization temperature.

Stiffler et al. [Sti91], using transient reflectivity and conductivity measurements, empirically derived undercooling values for these systems and found them to be 490 ± 40 K for a 400 nm-thick films on a 330 nm-thick SiO_2 layer on single-crystal Si substrate. Samples in this work were 400 nm-thick films on SiO_2 substrates, but it has been shown [Via94] that the thermal effect of the underlying single-crystal Si diminishes substantially (>90%) at intermediate SiO_2 layer thicknesses > 250 nm.

Using the undercooling value given by Stiffler et al. and equation (5.10) gives a solidification velocity of at least 18 m/s. This value cannot be accurate because it has been shown [Gal85] that solidification velocities in excess of 15 m/s

result in an amorphous microstructure. It is speculated that the undercooling values are less than Stiffler et al. have derived, and are actually closer to 200-300 K. These values lead to solidification velocities on the order of 8-12 m/s. Numerical derivations of velocity values from transient conductance data [Pee87] reveal that the highest u values occur just after solidification begins. This is not the case in this system due to the high thermal gradient with the undercooled center region. The gradient has its highest value just before bulk nucleation occurs, which is at ~ 100 ns, as outlined below. However, the solidifying front velocity is affected by the heat released by solidification ($u\Delta H$), which increases the temperature just ahead of the solidification interface.

At this point, the edge grain continues solidifying into the undercooled center region. Assuming an undercooling value of 250 K, the center region reaches the homogeneous nucleation temperature at ~ 55 -60 ns, according to the simulation. However, there is disparity with the empirical data regarding when bulk nucleation occurs, as transient conductance and reflectance data [Sti91] show bulk nucleation occurring at ~ 100 -120 ns. The empirical observation is presumably more accurate, and the disparity likely arises from the difference in undercooling values for the simulation and those calculated

using estimated quench rates. Therefore, the next temperature profile shown is for time = 120 ns in Figure 5-7(b).

Transient measurements [Sti90] show bulk nucleation occurring at ~ 120 ns, followed by rapid growth into the highly cooled liquid. This process releases enthalpy, reheating the film to the equilibrium melt temperature. This recalescence period takes ~ 10-20 ns.

At this point, shown in Figure 5-8(a), the center region is solidifying. A microstructural model [Sti91] describes this region as a randomly distributed crystalline inclusions in a continuous liquid matrix. The model has been confirmed with in situ measurements and subsequent microstructural analysis. The region where the inner grain grows is still molten due to lack of nucleation in the area. However, the solidifying center region provides a nucleation point and the thermal gradient created by heat loss to the large edge grain drives the solidification of the inner outward. This is shown in Figure 5-8 (b). This process results in the microstructure shown in Figure 4-26.

Anomalous Microstructures

Now that the general solidification model has been formulated, it is possible to speculate on the microstructural evolution of the anomalous regions, shown in Figures 4-8, 4-10, and 4-27. These samples have enlarged edge-type growth

occurring well into the center region where usually only a standard microstructure is observed. It appears that complete melting did not take place in these films and nucleation occurred in atypical regions. For example, Figure 4-10 shows an anomalous spherical region where the inner grains are typically observed. Here, however, a distinct nucleation point occurred, causing a perturbation that disrupted the standard microstructural evolution. It is speculated that a nanocrystalline cluster did not melt during irradiation and created a nucleation point. This type of event would occur at the equilibrium melt temperature just after the pulse is over, thereby disrupting the evolution early enough so that the center region is affected. Instead of severe undercooling and homogeneous nucleation, large grains nucleated and grew in a sequential fashion due to the anomalous nucleation event.

Non-contact Samples

Though microstructures observed for lower laser energy density ($< 350 \text{ mJ/cm}^2$) non-contact samples varied substantially from the contact counterparts, higher laser energy density ($> 350 \text{ mJ/cm}^2$) did not. Figure 4-16 shows a complete view of the irradiated region of a non-contact sample. This microstructure is the same as that modeled in this work, except for the surface energy effects that distorted the center of the edges. SEM analysis (Figure 4-28)

of these samples show a thickening of the edges due to surface tension. This type of effect has been observed previously [Sam93] in laser irradiation of a-Si islands on SiO₂ substrates. Edge regions would undergo thickness increases, resulting in a pile up of thermal energy. The increase in thickness decreased cooling rates and affected melt durations. This distortion of the surface topography is undesirable, from a technological standpoint, diminishing interest in this particular configuration of the laser-annealing technique.

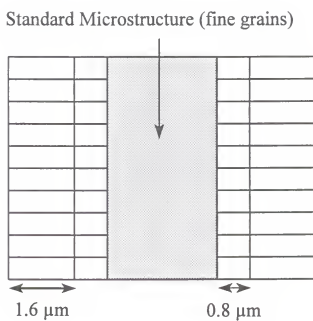


Figure 5-1 Schematic of microstructure used as a reference for the development of the model.

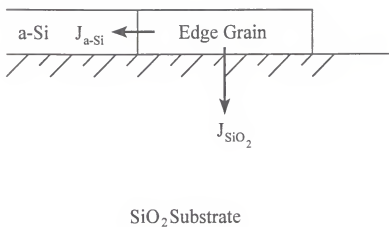


Figure 5-2 Schematic of microstructure used as a reference for the development of the model.

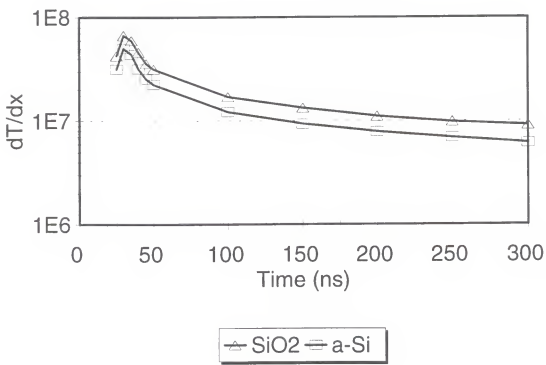


Figure 5-3 Calculated thermal gradient values as a function of time for amorphous silicon and SiO_2 substrates.

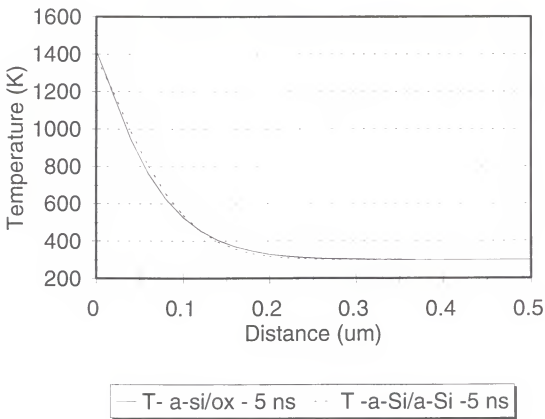


Figure 5-4 Calculated temperature profiles at $t = 5$ ns for amorphous Si on a (i) SiO_2 and (ii) amorphous Si substrate.

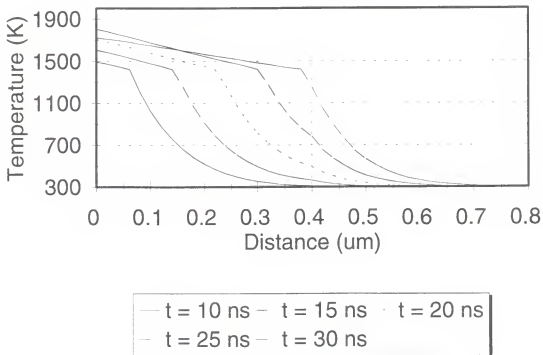
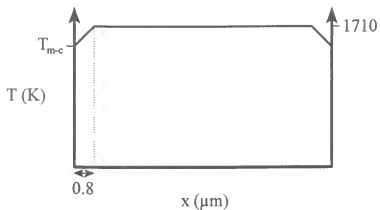
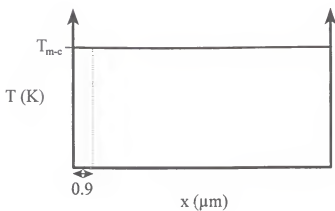


Figure 5-5 Calculated temperature profiles for various times of an amorphous Si film irradiated with a 700 mJ/cm^2 , 25 ns (FWHM) laser pulse.

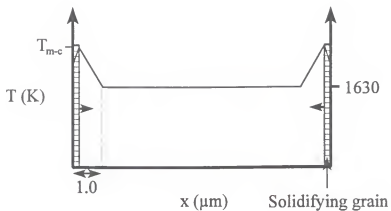


(a) Time = 30.5 ns

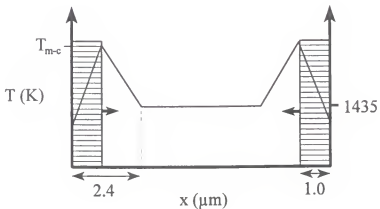


(b) Time = 32 ns

Figure 5-6 Schematic of temperature profiles at times of (a) 30 ns and (b) 32 ns for the microstructural evolution model.

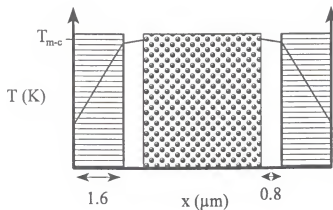


(a) Time = 35 ns

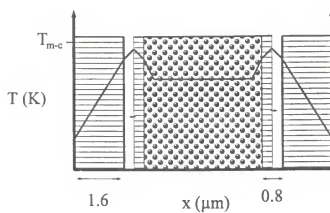


(b) Time = 120 ns

Figure 5-7 Schematic of temperature profiles at times of (a) 35 ns and (b) 120 ns for the microstructural evolution model. Thermal diffusion distances and edge grain growth are included.



(a) After recalescence



(b) Final solidification

Figure 5-8 Schematic of temperature profiles of (a) after recalescence and (b) final solidification.

CHAPTER 6 CONCLUSIONS

Amorphous silicon films deposited on high-quality fused-silica wafers were crystallized using an excimer laser. Two unique configurations were used for the crystallization process. They were (i) through-the substrate irradiation using special seed wafers in contact with the film surface, and (ii) selective -area crystallization using surface masking of the film during standard laser irradiation. The resultant microstructure of the films was then characterized by transmission electron microscopy (TEM) and scanning electron microscopy (SEM).

Samples processed using the seed method resulted in structures in which the film in contact with the seed delaminated, leaving behind a unique microstructure. Four distinct regions were observed, as a function of lateral distance from the contact area. Regions at least several microns away from the seed did not demonstrate any effect (grain size ~ 200 nm, no aspect ratio), but regions closer than that demonstrated enlarged growth (~ 1000 nm, aspect ratio 2:1) due to the nucleation effect caused by the seed.

Samples processed using selective-area crystallization of the film using surface masking resulted in one of three microstructures. Samples processed with the lower laser energy densities demonstrated a microstructure consistent with regular laser annealing (grain size ~ 200 nm, no aspect ratio). Samples processed with higher energy densities demonstrated either enlarged growth (factor of 3 greater than standard annealing), or anomalous growth (unusual aspect ratios or geometries).

APPENDIX
SIMULATION OF LASER INTERACTIONS WITH MATERIALS

A computer-based model, called SLIM (Simulation of Laser Interactions with Materials), has been developed by the author and his advisor, Rajiv Singh, at the University of Florida. SLIM is an implicit finite-difference method designed for accurate simulation of laser-irradiated materials on personal computer (PC) systems. The transient laser-induced effects include rapid surface heating, melting, vaporization, and resolidification in multi-layered structures.

The program is divided into two parts, INPUT and SLIM. The input program allows the user to create the input data file for running a simulation. Input information includes the temperature-dependent thermophysical properties (thermal conductivity, heat capacity, reflectivity, absorption coefficient) of the material, as well as temporally dependent properties of the laser (pulse shape, energy).

The second part of the program, SLIM, simulates the interactions, given the input data. Output data from SLIM includes surface temperature as a function of time, temperature profiles at any given time, melt depth as a function of time, and maximum melt and vaporization depths.

Table A1. Properties of amorphous, crystalline and liquid silicon used in the simulation.

Parameter	Material	Value and Reference
Density (g/cm ³)	c-Si	2.32 [Una89]
	a-Si	2.2 [Una89]
	l-Si	2.52 [Una89]
Melt latent heat (J/cm ³)	c-Si	4206 [Sin92]
	a-Si	2901 [Una89]
Melt Temperature (K)	c-Si	1685 [Sin92]
	a-Si	1420 [Sti91]
Reflectivity	c-Si	0.66 [Una89]
	a-Si	0.55 [Una89]
	l-Si	0.685 [Una89]
Absorption Coefficient (cm ⁻¹)	c-Si	1.7×10^6 [Una89]
	a-Si	1.5×10^6 [Una89]
	l-Si	1.56×10^6 [Una89]
Thermal Conductivity (W/cm·K)	c-Si	$1.6 \times 10^{-3} T^{-1.2}$ [Sin92]
	a-Si	$2.5 \times 10^{-5} T + 0.018$ [Fog93]
	l-Si	0.7 [Sin92]
Heat Capacity (J/cm ³ ·K)	c-Si	$1.92 + 2.54 \times 10^{-4} T$ [Sin92]
	a-Si	$2.4 \times 10^{-4} T + 2.2$ [Una89]
	l-Si	2.4 [Sin92]

Table A2. Properties of SiO_2 used in the simulation.

Parameter	Value and Reference
Density (g/cm ³)	2.2 [Una89]
Thermal Conductivity (W/cm·K)	$1.5 \times 10^{-5} T + 0.0084$ [Fog93]
Heat Capacity (J/cm ³ ·K)	$1.35 \times 10^{-4} T$ [Fog93]

LIST OF REFERENCES

All80 M. von Allmen, *Laser and Electron Beam Processing of Materials*, Ed. by C.W. White and P.S. Peercy (Academic Press, New York, 1980).

Ask89 D. Askeland, *The Science and Engineering of Materials*, 2nd Edition (PWS-Kent Publishing, Boston, 1989).

Aus78 D.H. Auston, C.M. Surko, T.N.C. Venkatesan, R.E. Slusher, J.A. Golovchenko, *Appl. Phys. Lett.* **33**, 437 (1978).

Bac90 R.Z. Bachrach, K. Winer, J.B. Boyce, S.E. Ready, R.I. Johnson, G.B. Anderson, *J. Elec. Mats.* **19**, 241 (1990).

Bac94 R.Z. Backrach, K. Winer, J.B. Boyce, F.A. Ponce, S.E. Ready, R. Johnson and G.B. Anderson, *Mater. Res. Symp. Proc.* **158**, 467 (1994).

Boh96 P. Boher, J.L. Stehle, M. Stehle, B. Godard, *Appl. Surf. Sci.* **96**, 376 (1996).

Bon91 M. Bonnel, N. Duhamel, M. Guendouz, L. Haji, B. Loisel, P. Ruault, *Jpn. J. Appl. Phys.* **30**, L1924 (1991).

Bou92 S. Boultadakis, S. Logothetidis, S. Ves, *J. Appl. Phys.* **72**, 3648 (1992).

Bra79 A. Brau, "Rare Gas Halogen Excimers", *Topics in Applied Physics*, Vol 30, Ed. by C.K. Rhodes (Springer-Verlag, New York, 1979).

Bro70 M.H. Brodsky, R.S. Title, K. Weiser, G.D. Pettit, *Phys. Rev. B* **1**, 2632 (1970).

Bro93 S.D. Brotherton, D.J. McCulloch, J.B. Clegg, J.P. Gowers, *IEEE Trans. Elect. Devs.* **40**, 407 (1993).

Bru92 C.R. Brundle, C.A. Evans and S. Wilson, Eds., *Encyclopedia of Materials Characterization* (Butterworth-Heinemann, Boston, 1992).

Buc94 K. Bucher, J. Bruns, H.G. Wagemann, *J. Appl. Phys.* **75**, 1127 (1994).

Cab91 P.R.I. Cabarrocas, P. Morin, V. Chu, J.P. Conde, J.Z. Liu, H.R. Park, S. Wagner, *J. Appl. Phys.* **69**, 2942 (1991).

Cha89 Y.J. Chabal, G.S. Higashi, K. Raghavachan, V.A. Burrows, *J. Vac. Sci. Tech.* **A7**, 2104 (1989).

Cho94a D. Choi, M. Matsumura, *Jpn. J. Appl. Phys.* **33**, L83 (1994).

Cho94b D. Choi, E. Sadayuki, O. Sugiura, M. Matsumura, *Jpn. J. Appl. Phys.* **33**, 70 (1994).

Chr94 D.B. Chrisey, *Pulsed Laser Deposition of Thin Films*, Ed. by G.K. Hubler (John Wiley & Sons, New York, 1994).

Cul82 A.G. Cullis, H.C. Webber, N.G. Chew, J.M. Poate, P. Baeri, *Phys. Rev. Lett.* **49**, 219 (1982).

Dev85 G. Devaud, D. Turnbull, *Appl. Phys. Lett.* **46**, 844 (1985).

Dye93 T.E. Dyer, J.M. Marhsall, W. Pickin, A.R. Hepburn, J.F. Davies, *J. Non-Cryst. Sol.* **164**, 1001 (1993).

Edw85 D.F. Edwards, *Handbook of Optical Constants of Solids*, Ed. by E.D. Palik (Academic Press, New York, 1985).

Fog93 E. Fogarassy, *Appl. Surf. Sci.* **69**, 231 (1993).

Fri92 M. Fried, T. Lohner, W.A.M. Aarnink, L.J. Hanekamp, A.V. Silfhout, *J. Appl. Phys.* **71**, 5260 (1992).

Gal81 G.J. Galvin, M.O. Thompson, J.W. Mayer, R.B. Hammond, N. Paultre, P.S. Peercy, *Phys. Rev. Lett.* **48**, 33 (1981).

Gal85 G.J. Galvin, J.W. Mayer, P.S. Peercy, *Appl. Phys.*

Lett. **46**, 644 (1985).

Gri93 C.P. Grigoropoulos, A.A. Rostami, X. Xu, S.L. Taylor, H.K. Park, Int. J. Heat Mass Transfr. **36**, 1219 (1993).

Haj94 L. Haji, P. Joubert, J. Stoemenos, N.A. Economou, J. Appl. Phys. **75**, 3944 (1994).

Hat87 M.K. Hatalis and D.W. Greve, IEEE Elect. Dev. Lett. **EDL-8**, 361 (1987).

Hig90 G.S. Higashi, Y.J. Chabal, G.W. Trucks, K. Raghavachari, Appl. Phys. Lett. **56**, 656 (1990).

Hof79 P.W. Hoff and C.K. Rhodes, "Introduction", *Topics in Applied Physics*, Vol 30, Ed. by C.K. Rhodes (Springer-Verlag, New York, 1979).

Hol92 L. Holz, A. Semjonow, K. Lenz, A. Lau, W. Richter, H. Wilhelm, J. Appl. Phys. **72**, 2472 (1992).

Hum85 R.E. Hummel, *Electronic Properties of Materials*, (Springer-Verlag, New York 1985).

Im93 J.S. Im, H.J. Kim, M.O. Thompson, Appl. Phys. Lett. **63**, 1969 (1993).

Im94 J.S. Im, H.J. Kim, Appl. Phys. Lett. **64**, 2302 (1994).

Ish95 R. Ishihara, W. Yeh, T. Hattori, M. Matsumura, Jpn. J. Appl. Phys. **34**, 1759 (1995).

Ive85 R.B. Iverson, R. Reif, J. Appl. Phys. **57**, 5169 (1985).

Ive87 R.B. Iverson, R. Reif, J. Appl. Phys. **62**, 1675 (1987).

Jae90 R.C. Jaeger, *Introduction to Microelectronic Fabrication*, Vol. V, Eds. G.W. Neudeck, R.F. Pierret (Addison-Wesley, Reading, Mass. 1990).

Jel82 G.E. Jellison, F.A. Modine, Appl. Phys. Lett. **41**, 180 (1982).

Jeo89 *JEOL News*, JEOL News Editorial Board, JEOL LTD, Akishima, Tokyo, Japan.

Kak89 R. Kakkad, J. Smith, W. S. Lau, S.J. Fonash, J.

Appl. Phys. **65**, 2069 (1989).

Kam88 T. Kamins, *Polysilicon for Integrated Circuit Application* (Kluwer, Boston, 1988).

Hat87 M. K. Hatalis and D.W. Greve, IEEE Elect. Dev. Lett. **EDL-8**, 361 (1987).

Kin94 T.J. King, M.G. Hack, I.W. Wu, J. Appl. Phys. **75**, 908 (1994).

Kum94 H. Kumomi, T. Yonehara, J. Appl. Phys. **75**, 2884 (1994).

Kun91 M. Kunst, H.C. Neitzert, J. Appl. Phys. **69**, 8320 (1991).

Kuri93 H. Kuriyama, T. Nohda, S. Ishida, T. Kuwahara, S. Noguchi, S. Kiyama, S. Tsuda, S. Nakano, Jpn. J. Appl. Phys. **32**, 6190 (1993).

Kurz87 H. Kurz, Mater. Res. Symp. Proc. **74**, 3 (1987).

Lar88 B.C. Larson, J. Z. Tischler, D.M. Mills, Mater. Res. Symp. Proc. **100**, 513 (1988).

Liu79 P.L. Liu, R. Yen, N. Bloembergen, R.T. Hodgson, Appl. Phys. Lett. **34**, 864 (1979).

Low83 D.H. Lowndes, R.F. Wood, R.D. Westbrook, Appl. Phys. Lett. **43**, 258 (1983).

Low84 D.H. Lowndes, R.F. Wood, J. Narayan, Phys. Rev. Lett. **52**, 561 (1984).

Lyn85 D.W. Lynch, *Handbook of Optical Constants of Solids*, Ed. by E.D. Palik, (Academic Press, New York, 1985).

May73 J. Maya, P. Davidovits: J. Chem. Phys. **59**, 3143 (1973)

Mor89 Y. Morita, T. Noguchi, Jpn. J. Appl. Phys. **28**, L309 (1989).

Nak91 K. Nakazawa, J. Appl. Phys. **69**, 1703 (1991).

Nar84a J. Narayan, C.W. White, O.W. Holland, M.J. Aziz, J. Appl. Phys. **56**, 1821 (1984).

Nar84b J. Narayan, C.W. White, *Appl. Phys. Lett.* **44**, 35 (1984).

Nar85 J. Narayan, C.W. White, M.J. Aziz, B. Stritzker, A. Walthuis, *J. Appl. Phys.* **57**, 564 (1985).

Nom91 T. Noma, T. Yonehara, H. Kumomi, *Appl. Phys. Lett.* **59**, 653 (1991).

Ohr92 M. Ohring, *The Materials Science of Thin Films*, (Academic Press, San Diego, 1992).

Ols85 G.L. Olson, *Mater. Res. Symp. Proc.* **35**, 25 (1985).

Oma93 W.C. Omara, "Liquid Crystal Displays" in *Manufacturing Science and Technology* (Van Nostrand and Reinhold, New York, 1993).

Ong88 C.K. Ong, H.S. Tan, E.H. Sin, *Mat. Sci. Eng.* **A103**, 273 (1988).

Pee87 P.S. Peercy, M.O. Thompson, J.Y. Tsao, *Mater. Res. Symp. Proc.* **74**, 15 (1987).

Pil85 H. Piller, *Handbook of Optical Constants of Solids*, Ed. by E. D. Palik (Academic Press, New York, 1985).

Poa82 J.M. Poate and J.W. Mayer, *Laser Annealing of Semiconductors*, Ed. by J.M. Poate and J.W. Mayer, (Academic Press, New York, 1982).

Rea63 J.F. Ready, *Appl. Phys. Lett.* **3**, 11 (1963).

Rea71 J.F. Ready, *Effects of High Power Laser Radiation* (Academic Press, New York, 1971).

Sag89 K. Sagara, E. Murakami, *Appl. Phys. Lett.* **54**, 2003 (1989).

Sak91 A. Sakai, H. Ono, K. Ishida, T. Niino, T. Tatsumi, *Jpn. J. Appl. Phys.* **30**, L941 (1991).

Sak92 J. Sakurai, Y. Uno, Y. Sato, H. Hiji, S. Kyozuka, T. Suzuki, and T. Ozawa, in *Technical Digest of the Society for Information and Display Symposium*, **17**, 344, Boston, (1992).

Sam86 T. Sameshima, S. Usui, *Mater. Res. Symp. Proc.* **71**,

435 (1986).

Sam87 T. Sameshima, S. Usui, H. Tomita, Jpn. J. Appl. Phys. **26**, L1678 (1987).

Sam89 T. Sameshima, M. Hara, S. Usui, Jpn. J. Appl. Phys. **28**, 1789 (1989).

Sam91 T. Sameshima, S. Usui, J. Appl. Phys. **70**, 1281 (1991).

Sam93 T. Sameshima, S. Usui, J. Appl. Phys. **74**, 6592 (1993).

Sea79 C.H. Seager, D.S. Ginley, Appl. Phys. Lett. **34**, 337 (1979).

Sel94 M. Seliya, M. Hara, N. Sano, A. Kohno, T. Sameshima, IEEE Elect. Dev. Lett. **15**, 69 (1994).

Sera89 K. Sera, F. Okumura, H. Uchida, S. Itoh, S. Kaneko, K. Hotta, IEEE Elect. Dev. Lett. **36**, 2868 (1989).

Seri89a T. Serikawa, S. Shirai, A. Okamoto, S. Suyama, IEEE Elect. Dev. Lett. **36**, 1929 (1989).

Seri89b T. Serikawa, S. Shirai, A. Okamoto, S. Suyama, Jpn. J. Appl. Phys. **28**, L1871 (1989).

Shi92a S. Shirai, K. Kimura, Y. Irita, N. Naito, T. Serikawa, S. Kohda, N. Yamauchi, and M. Yamaguchi, in Technical Digest of the Topical Meeting on Photonic Switching, **1**, 2A6, Minsk, (1992).

Shi92b S. Shirai, T. Serikawa, IEEE Elect. Dev. Lett. **39**, 450 (1992).

Sin92 R.K. Singh, J. Viatella, J. Metals, **44**, 20 (1992).

Sin96 R.K. Singh, D.R. Gilbert, J. Viatella, Mat. Sci. Eng. B **40**, 89 (1996).

Sir79 M.R.T. Siregar, M.V. Allmen, W. Luthy, Helvetica Physica Acta **52**, 45 (1979).

Sti88 S.R. Stiffler, M.O. Thompson, P.S. Peercy, Mater. Res. Symp. Proc. **100**, 505 (1988).

Sti91 S.R. Stiffler, M.O. Thompson, Phys. Rev. B **43**, 9851 (1991).

Suz94 T. Suzuki, S. Adachi, Jpn J. Appl. Phys. **33**, 5599 (1994).

Tak91 M. Takabatake, J. Ohwada, A. Ono, A. Mimura, and N. Konishi, IEEE Trans. Elect. Devs. **ED-38**, 1303 (1991).

Kan91 T. Kaneko, Y. Hosokawa, M. Tadauchi, Y. Kita, and H. Andoh, IEEE Trans. Elect. Devs. **ED-38**, 1086 (1991).

Tho84 M.O. Thompson, G.J. Galvin, J.W. Mayer, P.S. Peercy, J.M. Poate, D.C. Jacobson, A.G. Cullis, N.G. Chew, Phys. Rev. Lett. **52**, 2360 (1984).

Tsa87 J.Y. Tsao, P.S. Peercy, Phys. Rev. Lett. **58**, 2782 (1987).

Tsu79 R. Tsu, R.T. Hodgson, T.Y. Tan, J.E. Baglin, Phys. Rev. Lett. **42**, 1356 (1979).

Tsu93 T. Tsukada, J. Non-Cryst. Sol. **164**, 721 (1993).

Una89 S.D. Unamuno, E. Fogarassy, Appl. Surf. Sci. **36**, 1 (1989).

Ung84 T. Ungami and B.T Tsujiyama, Proc. Soc. Info. Display **25**, 117 (1984).

Vel76 J.E. Velazco, J.H. Koltz, D.W. Setser: J. Chem. Phys. **65**, 3468 (1976)

Via94 J. Viatella, R.K. Singh, R. Thakur, G. Sandhu, Mater. Res. Symp. Proc. 342, 297 (1994).

Via96 J. Viatella, R.K. Singh, Mat. Sci. Eng. B, to be published.

Wei86 B.R. Weinbereger, G.G. Peterson, T.C. Eschrich, and H.A. Kransinski, J. Appl. Phys. **60**, 3232 (1986).

Wil95 D.L. Williamson, S. Roorda, M. Chicoine, R. Tabti, P. A. Stolk, S. Acco, F. W. Saris, Appl. Phys. Lett. **67**, 226 (1995).

Win90 K. Winer, G.B. Anderson, S.E. Ready, R.Z. Bachrach, R.I. Johnson, F.A. Ponce, J.B. Boyce, *Appl. Phys. Lett.* **57**, 2222 (1990).

Woo81 R.F. Wood, G.E. Giles, *Phys. Rev. B* **23**, 2923 (1981).

Woo84a R.F. Wood, G.E. Jellison, Jr, *Melting Model of Pulsed Laser Processing* (Academic Press, New York, 1984).

Woo84b R.F. Wood, D.H. Lowndes, J. Narayan, *Appl. Phys. Lett.* **44**, 770 (1984).

Woo86 R.F. Wood, G.A. Geist, *Phys. Rev. B* **34**, 2606 (1986).

Xu94 X. Xu, C. P. Grigoropoulos, R. E. Russo, *Appl. Phys. Lett.* **65**, 1745 (1994).

Yamag93 M. Yamaguchi, Y. Kaneko, K. Tsutsui, *Jpn. J. Appl. Phys.* **32**, 458 (1993).

Yamu91 N. Yamauchi, J.J. Hajjar, R. Reif, *IEEE Trans. Elect. Devs.* **38**, 55 (1991).

Yamu94 N. Yamauchi, R. Reif, *J. Appl. Phys.* **75**, 3235 (1994).

BIOGRAPHICAL SKETCH

John Wade Viatella was born on December 22, 1966, in Cali, Colombia, S.A. He moved to the United States in 1975 and graduated from Atlantic High School in Delray Beach, Florida, in 1984. He began attending Florida Atlantic University in the fall of 1984 and continued there until fall of 1985. He transferred to Palm Beach Community College and completed his A.A. in the summer of 1988. In the fall of 1988 he enrolled at the University of Florida and completed his Bachelor of Science in Materials Science and Engineering in the summer of 1991. In the fall of 1991 he entered the graduate program at the University of Florida to begin his studies for a degree of Doctor of Philosophy in the field of materials science and engineering with a specialty in electronic materials.

I certify that I have read this study and that in my opinion it conforms to acceptable standards of scholarly presentation and is fully adequate, in scope and quality, as a dissertation for the degree of Doctor of Philosophy.

Rajiv Singh
Rajiv K. Singh, Chair
Professor of Materials
Science and Engineering

I certify that I have read this study and that in my opinion it conforms to acceptable standards of scholarly presentation and is fully adequate, in scope and quality, as a dissertation for the degree of Doctor of Philosophy.

Paul Holloway
Paul Holloway
Professor of Materials
Science and Engineering

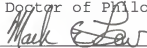
I certify that I have read this study and that in my opinion it conforms to acceptable standards of scholarly presentation and is fully adequate, in scope and quality, as a dissertation for the degree of Doctor of Philosophy.

Robert Park
Robert Park
Professor of Materials
Science and Engineering

I certify that I have read this study and that in my opinion it conforms to acceptable standards of scholarly presentation and is fully adequate, in scope and quality, as a dissertation for the degree of Doctor of Philosophy.

Steve Pearton
Steve Pearton
Professor of Materials
Science and Engineering

I certify that I have read this study and that in my opinion it conforms to acceptable standards of scholarly presentation and is fully adequate, in scope and quality, as a dissertation for the degree of Doctor of Philosophy.



Mark Law

Professor of Electrical
and Computer Engineering

This dissertation was submitted to the Graduate Faculty of the College of Engineering and to the Graduate School and was accepted as partial fulfillment of the requirements for the degree of Doctor of Philosophy.

May, 1997



Winfred M. Phillips
Dean, College of
Engineering

Karen A. Holbrook
Dean, Graduate School